



Deciphering the Local Interstellar Spectra of Secondary Nuclei with the Galprop/Helmod Framework and a Hint for Primary Lithium in Cosmic Rays

M. J. Boschini^{1,2} , S. Della Torre¹ , M. Gervasi^{1,3} , D. Grandi^{1,3} , G. Jøhannesson^{4,5} , G. La Vacca^{1,3} , N. Masi⁶ , I. V. Moskalenko^{7,8} , S. Pensotti^{1,3} , T. A. Porter^{7,8} , L. Quadrani^{6,9} , P. G. Rancoita¹ , D. Rozza^{1,3} , and M. Tacconi^{1,3}

¹ INFN, Milano-Bicocca, Milano, Italy

² CINECA, Segrate, Milano, Italy

³ Physics Department, University of Milano-Bicocca, Milano, Italy

⁴ Science Institute, University of Iceland, Dunhaga 3, IS-107, Reykjavik, Iceland

⁵ NORDITA, Roslagstullsbacken 23, SE-106 91, Stockholm, Sweden

⁶ INFN, Bologna, Italy

⁷ Hansen Experimental Physics Laboratory, Stanford University, Stanford, CA 94305, USA

⁸ Kavli Institute for Particle Astrophysics and Cosmology, Stanford University, Stanford, CA 94305, USA

⁹ Physics Department, University of Bologna, Bologna, Italy

Received 2019 November 8; revised 2019 December 11; accepted 2019 December 12; published 2020 February 4

Abstract

Local interstellar spectra (LIS) of secondary cosmic-ray (CR) nuclei, lithium, beryllium, boron, and partially secondary nitrogen, are derived in the rigidity range from 10 MV to ~ 200 TV using the most recent experimental results combined with state-of-the-art models for CR propagation in the Galaxy and in the heliosphere. The lithium spectrum appears somewhat flatter at high energies compared to other secondary species, which may imply a primary lithium component. Two propagation packages, GALPROP and HELMOD, are combined to provide a single framework that is run to reproduce direct measurements of CR species at different modulation levels, and at both polarities of the solar magnetic field. An iterative maximum-likelihood method is developed that uses GALPROP-predicted LIS as input to HELMOD, which provides the modulated spectra for specific time periods of the selected experiments for the model-data comparison. The proposed LIS accommodates the low-energy interstellar spectra measured by *Voyager 1*, the *High Energy Astrophysics Observatory-3 (HEAO-3)*, and the Cosmic Ray Isotope Spectrometer on board of the *Advanced Composition Explorer (ACE/CRIS)*, as well as the high-energy observations by the *Payload for Antimatter Matter Exploration and Light-nuclei Astrophysics (PAMELA)*, *Alpha Magnetic Spectrometer-02 (AMS-02)*, and earlier experiments that are made deep in the heliosphere. The interstellar and heliospheric propagation parameters derived in this study are consistent with our earlier results for propagation of CR protons, helium, carbon, oxygen, antiprotons, and electrons.

Unified Astronomy Thesaurus concepts: [Cosmic rays \(329\)](#); [Heliosphere \(711\)](#); [Interstellar medium \(847\)](#); [Interplanetary medium \(825\)](#); [Particle astrophysics \(96\)](#); [Isotopic abundances \(867\)](#)

Supporting material: machine-readable tables

1. Introduction

Cosmic rays (CRs) are the only pieces of matter available to us that come from large Galactic and extragalactic distances. Their spectrum and composition provide invaluable information about their origin and propagation history. The bulk of Galactic CRs is associated with the most energetic events such as supernova explosions, but some fraction may also come from pulsars, interstellar shocks, neutron star mergers, and perhaps from even more exotic and less studied processes. The origin of extragalactic CRs is still a mystery, with speculations ranging from nuclei of active galaxies to gamma-ray bursts and primordial shocks.

Virtually all hydrogen ^1H and most helium ^4He were produced in the first minutes after the Big Bang alone, with trace amounts of deuterium ^2H , light helium isotope ^3He , and ^7Li . Almost all other varieties of nuclei species are the result of stellar thermonuclear burning and explosive nucleosynthesis. This material is then mixed into the interstellar medium, fragmented, and reprocessed by energetic CR particles interacting with the interstellar gas. The new shocks propagating through such a mixture accelerate all available species producing fresh CRs that are mixing with older CRs produced by supernova remnants, which went off millions of years ago when the human race did not even exist yet.

Although fragmentation of CR species does not play a major role in the chemical evolution of the Galaxy, it is the main source of isotopes that are not synthesized in stars or depleted in the process of thermonuclear burning. These kinds of nuclides are isotopes of Li, Be, and B, which are called secondary. Fragmentation of CR nuclei also produces all other isotopes that make the composition of CRs noticeably different from the composition of their sources and the interstellar matter. For instance, the amounts of primary and secondary nitrogen in CRs are about equal. The relative amounts and spectra of those so-called secondary isotopes reflect the processes of their production as well as their acceleration and propagation history. Therefore, studies of CR composition and spectra are able to shed light on the global properties and history of our Galaxy, CR sources, and acceleration processes, and properties of the components of the interstellar medium (e.g., interstellar gas distribution, spectrum of turbulence, etc.).

The observed abundances of stable secondary CR nuclei (e.g., ^3He , Li, Be, B, Sc, Ti, V) and radioactive isotopes with half-lives of ~ 1 Myr (^{10}Be , ^{26}Al , ^{36}Cl , ^{54}Mn) allow the determination of the Galactic halo size and diffusion coefficient (Ptuskin & Soutoul 1998; Strong & Moskalenko 1998, 2001; Webber & Soutoul 1998; Moskalenko et al. 2001; Trotta et al. 2011;

Jóhannesson et al. 2016). K-capture isotopes in CRs (e.g., ^{49}V , ^{51}Cr) can be used to study energy-dependent effects (Soutoul et al. 1998; Jones et al. 2001; Niebur et al. 2003) such as diffusive reacceleration because their lifetime depends on the rates of electron attachment and stripping in the interstellar gas. Trans-iron CR nuclei abundances ($Z \geq 29$) are an invaluable source of information about our local environment. Their large fragmentation cross sections (e.g., see Figure 1 in Wellisch & Axen 1996) imply that they originate in local sources.

Most of these measurements are done at low energies deep inside the heliosphere, where the solar modulation is significant. Meanwhile, many parameters of the interstellar propagation models are derived using these low-energy measurements, which are then extrapolated to TeV energies and above. Such models, in turn, are used for interpretation of data of CR missions and space telescopes and to search for signatures of new physics. Therefore, the determination of the true local interstellar spectra (LIS) of secondary species, Li, Be, B, is of considerable interest for the astrophysics and particle physics communities.

In this paper, we use an updated version of a 2D Monte Carlo code for heliospheric propagation HELMOD (Boschini et al. 2018c, 2019), combined with the latest version (56) of the interstellar propagation code GALPROP (Porter et al. 2017; Jóhannesson et al. 2018) to take advantage of significant progress in CR measurements to derive the LIS for Li, Be, and B. The HELMOD model solves the Parker equation (Parker 1965) and includes all relevant effects, including a full description of the diffusion tensor. Our method and approach are described in a series of recent papers devoted to the LIS of CR p , \bar{p} , e^- , and He, C, O nuclei (Boschini et al. 2017, 2018a, 2018b).

2. CR Transport in the Galaxy and the Heliosphere

Here we provide short descriptions of the two dedicated codes that are used in the present work and that complement each other: GALPROP¹⁰—for description of the interstellar propagation, and HELMOD¹¹—for description of the heliospheric transport. More details can be found in the referenced papers.

2.1. GALPROP Model for Galactic CR Propagation and Diffuse Emission

The state-of-the-art propagation code GALPROP is widely employed for modeling of CRs and associated emissions from the Milky Way, and now has about 23 years of development behind it (Moskalenko & Strong 1998; Strong & Moskalenko 1998). The GALPROP code uses information from astronomy, particle, and nuclear physics to predict CRs, γ -rays, synchrotron emission and its polarization in a self-consistent manner—it provides the modeling framework unifying many results of individual measurements in physics and astronomy spanning in energy coverage, types of instrumentation, and the nature of detected species. The GALPROP code range of physical validity covers sub-keV—PeV energies for particles and from 10^{-6} eV—PeV for photons. Over the years the project has been widely recognized as a standard modeling tool for Galactic CR propagation and associated diffuse emissions (radio, X-rays, γ -rays). The GALPROP code is *public* and is extensively used by

many experimental groups, and by thousands of individual researchers worldwide for interpretation of their data and for making predictions.

The key concept underlying the GALPROP code is that various kinds of data, e.g., direct CR measurements, \bar{p} , e^\pm , γ -rays, synchrotron radiation, and so forth, are all related to the same Galaxy and hence have to be modeled self-consistently (Moskalenko et al. 1998). The goal for the GALPROP-based models is to be as realistic as possible and to make use of available astronomical information, nuclear and particle data, with a minimum of simplifying assumptions (Strong et al. 2007).

The GALPROP code (Strong & Moskalenko 1998) solves a system of about 90 transport equations (time-dependent partial differential equations in 3D or 4D: spatial variables plus energy) with a given source distribution and boundary conditions for all CR species (^1H – ^{64}Ni , \bar{p} , e^\pm). This includes convection, distributed reacceleration, energy losses, nuclear fragmentation, radioactive decay, and production of secondary particles and isotopes. The numerical solution is based on a Crank–Nicholson implicit second-order scheme (Press et al. 1992). The spatial boundary conditions assume free particle escape. For a given halo size the diffusion coefficient, as a function of momentum and propagation parameters, is determined from secondary-to-primary nuclei ratios, typically B/C, [Sc+Ti+V]/Fe, and/or \bar{p}/p . If reacceleration is included, the momentum-space diffusion coefficient D_{pp} is related to the spatial coefficient D_{xx} ($=\beta D_0 R^\delta$) (Seo & Ptuskin 1994), where $\delta = 1/3$ for a Kolmogorov spectrum of interstellar turbulence or $\delta = 1/2$ for an Iroshnikov–Kraichnan cascade, R is the magnetic rigidity.

The injection spectra of CR species are parameterized by the rigidity-dependent function:

$$q(R) \propto (R/R_0)^{-\gamma_0} \prod_{i=0}^2 [1 + (R/R_i)^{\frac{\gamma_i - \gamma_{i+1}}{s_i}}]^{s_i}, \quad (1)$$

where $\gamma_{i=0,1,2,3}$ are the spectral indices, $R_{i=0,1,2}$ are the break rigidities, and s_i are the smoothing parameters (s_i is negative/positive for $|\gamma_i| \leq |\gamma_{i+1}|$).

The GALPROP code computes a complete network of primary, secondary, and tertiary CR production starting from input source abundances. GALPROP includes K-capture, electron pickup, and stripping processes (Pratt et al. 1973; Wilson 1978; Crawford 1979), and knock-on electrons (Abraham et al. 1966; Berrington & Dermer 2003). Cross sections are based on the extensive LANL database, nuclear codes, and parameterizations (Mashnik et al. 2004; see also a compilation in Génolini et al. 2018). The most important isotopic production cross sections are calculated using our fits to major production channels (Moskalenko & Mashnik 2003; Moskalenko et al. 2003; Génolini et al. 2018). Other cross sections are computed using phenomenological codes (Silberberg et al. 1998; Webber et al. 2003) renormalized to the data where they exist. The nuclear reaction network is built using the Nuclear Data Sheets.

GALPROP calculates production of secondary particles in pp -, pA -, Ap -, AA -interactions. Calculations of \bar{p} production and propagation are detailed in Moskalenko et al. (2002, 2003), and Kachelriess et al. (2015, 2019). Production of neutral mesons (π^0 , K^0 , \bar{K}^0 , etc.), and secondary e^\pm is calculated using the formalism by Dermer (1986a, 1986b), as described in Moskalenko & Strong (1998), or recent parameterizations by Kamae et al. (2006), Kachelriess & Ostapchenko (2012), and Kachelriess et al. (2014, 2019). γ -ray production and synchrotron emission are calculated

¹⁰ Available from <http://galprop.stanford.edu>.

¹¹ <http://www.helmod.org/>

using the propagated CR distributions, including primary e^- , secondary e^\pm , and for γ -rays—including secondary p from inelastic processes (Strong et al. 2004, 2010; Porter et al. 2008; Orlando & Strong 2013).

More details on GALPROP, including the description of all involved processes and reactions, can be found in dedicated publications (Moskalenko & Jourdain 1997; Moskalenko & Strong 1998, 2000; Strong & Moskalenko 1998; Strong et al. 2000, 2004, 2007, 2010, 2011; Moskalenko et al. 2002, 2003, 2017; Ptuskin et al. 2006b; Vladimirov et al. 2011, 2012; Orlando & Strong 2013; Porter et al. 2017, 2019; Jóhannesson et al. 2018, 2019; Génolini et al. 2018).

2.2. HELMOD Model for Heliospheric Transport

The combined effects of the intense solar wind and solar magnetic field modify the local interstellar space and develop a bubble-like structure, known as the heliosphere, that surrounds the whole solar system. The heliosphere affects the propagation of CR particles up to ~ 50 GV in rigidity and requires a dedicated modeling to understand all factors involved (see the discussion in Boschini et al. 2017). CR propagation in the heliosphere was first studied by Parker (1965), who formulated the transport equation also known as the Parker equation (see, e.g., discussion in Bobik et al. 2012, and references therein):

$$\frac{\partial U}{\partial t} = \frac{\partial}{\partial x_i} \left(K_{ij}^S \frac{\partial U}{\partial x_j} \right) + \frac{1}{3} \frac{\partial V_{sw,i}}{\partial x_i} \frac{\partial}{\partial T} (\alpha_{rel} T U) - \frac{\partial}{\partial x_i} [(V_{sw,i} + v_{d,i}) U], \quad (2)$$

where U is the number density of CR species per unit of kinetic energy T , t is the time, $V_{sw,i}$ is the solar wind velocity along the axis x_i , K_{ij}^S is the symmetric part of the diffusion tensor, $v_{d,i}$ is the particle magnetic drift velocity (related to the antisymmetric part of the diffusion tensor), and finally $\alpha_{rel} = \frac{T + 2m_r c^2}{T + m_r c^2}$, with m_r being the particle rest mass in units of GeV/nucleon. Parker's transport equation describes: (i) the *diffusion* of CR species due to magnetic irregularities, (ii) the so-called *adiabatic-energy changes* associated with expansions and compressions of cosmic radiation, (iii) an *effective convection* resulting from the convection with *solar wind* (SW, with velocity V_{sw}), and (iv) the drift effects related to the *drift velocity* (v_d).

The influence of heliospheric propagation on the spectra of CR species is called the solar modulation. Its overall effect leads to the suppression of the low-energy part in the spectra of CR species, while the amplitude of the suppression depends on the solar activity, particle charge sign, polarity of the solar magnetic field, and other conditions. In this work, the particle transport within the heliosphere is treated using the HELMOD model (Boschini et al. 2019, and reference therein). The HELMOD model, now version 4.0, numerically solves the Parker (1965) transport equation using a Monte Carlo approach involving stochastic differential equations (see a discussion in, e.g., Bobik et al. 2012, 2016). The particle transport within the heliosphere is computed from the outer boundary (i.e., the heliopause) down to Earth's orbit. In the latest version the actual dimensions of the heliosphere and its boundaries were taken into account based on *Voyager 1* measurements (Boschini et al. 2019).

The heliopause (HP) represents the extreme limit beyond which solar modulation does not affect CR flux. Thus, the CR spectra measured by *Voyager 1* outside HP are the truly pristine LIS of CR species.¹² Using Parker's model of the heliosphere (Parker 1961, 1963) combined with *Voyager 1* observations, we were able to estimate the time dependence of positions of the termination shock (TS, R_{TS}) and the HP (R_{HP}) as (Boschini et al. 2019):

$$R_{TS} = R_{obs} \left(\frac{\rho_{obs} u_{obs}^2}{P_{ISM}} \right)^{\frac{1}{2}} \left[\frac{\gamma + 3}{2(\gamma + 1)} \right]^{\frac{1}{2}}. \quad (3)$$

$$\frac{R_{HP}}{R'_{TS}} = 1.58 \pm 0.05, \quad (4)$$

where ρ_{obs} and u_{obs} are respectively plasma density and plasma velocity measured in situ at distance R_{obs} , P_{ISM} is the stagnation pressure discussed in Section 4 of Boschini et al. (2019), and $\gamma = 5/3$. R'_{TS} is defined as the TS position at the time when it was left by the SW stream that is currently reaching the HP (for more details see Boschini et al. 2019); this typically takes about 4 yr, but depends on the SW speed. Therefore, the actual dimensions of the heliosphere used in HELMOD-4 evolve with time. The predicted TS distances are in good agreement with those observed: for *Voyager 1* (*Voyager 2*) the detected TS position is 93.8 au (83.6 au) and the predicted position is 91.8 au (86.3 au), i.e., within 3 au ($< 3.5\%$ error). Regarding the HP, based on the R_{HP} observed by *Voyager 1*, the predicted R_{HP} at the time of the *Voyager 2* crossing was 120.7 au, while in reality it is 119 au.

In the present code, particular attention is paid to the quality of description of the high solar activity periods, which is evaluated through a comparison of HELMOD calculations and the CR proton data by Alpha Magnetic Spectrometer (AMS-02; Aguilar et al. 2018a), and to transitions from/to solar minima. This was achieved through introduction of a drift suppression factor and particle diffusion parameters, which depend on the level of solar disturbances (see a discussion in Boschini et al. 2019).

2.3. Scenarios of a Spectral Break at 300 GV

In 2011 the Payload for Antimatter Matter Exploration and Light-nuclei Astrophysics (PAMELA) collaboration reported observation of a new break (hardening) in the spectra of the most abundant CR species, protons and He, above a rigidity of a few hundred GV (Adriani et al. 2011). This publication confirmed the hardening of the CR proton and He spectra found in earlier experiments, ATIC-2 (Wefel et al. 2008; Panov et al. 2009) and CREAM (Ahn et al. 2010; Yoon et al. 2011). Later, the break was also confirmed by the *Fermi-LAT* (Ackermann et al. 2014) and with much higher precision and statistics by AMS-02 (Aguilar et al. 2015a, 2015b). The break is smooth and observed at the same rigidity ~ 300 GV for both species.

The interpretations of the break started to appear soon after the PAMELA publication. Perhaps the first was a paper by Vladimirov et al. (2012), which offered three distinctly different scenarios that can be tested through precise measurements of secondary species, such as secondary nuclei and \bar{p} ,

¹² *Voyager 2* is now in interstellar space, confirming the data from its sister spacecraft *Voyager 1* (Stone et al. 2019).

and anisotropy measurements. The proposed interpretations include (i) the “propagation” (P) scenario, where the observed break is the result of a change in the spectrum of interstellar turbulence that translates into a break in the index of the diffusion coefficient, (ii) the “injection” (I) scenario, where the break is due to the presence of populations of CR sources injecting particles with softer and harder spectra, and (iii) the “local source” scenario, where the local source injects low- (L -) or high-energy (H -scenario) particles with the spectrum that is correspondingly softer or harder than the rest of CRs produced by distant sources.

The P -scenario implies that the break should be observed in spectra of all CR species at about the same rigidity since the interstellar turbulence acts on all particles. Thus, the index of the rigidity dependence of the diffusion coefficient δ has to have a break at the same rigidity, where its values δ_1 below and δ_2 above the break are connected with the observed value of the break $\Delta\alpha$ in the spectral index of *propagated* primary species: $\delta_2 = \delta_1 - \Delta\alpha$, where $\Delta\alpha = \alpha_1 - \alpha_2$, and α_1 (α_2) is the observed spectral index of primaries below (above) the break. The observed spectrum of secondary species has an index $\epsilon_1 = \alpha_1 + \delta_1$ below the break and an index $\epsilon_2 = \alpha_2 + \delta_2 = \alpha_1 + \delta_1 - 2\Delta\alpha$ above the break. Therefore, the change in the spectral index of secondary species would be $\Delta\epsilon = \epsilon_1 - \epsilon_2 = 2\Delta\alpha$, i.e., twice the value of the break observed in the spectra of primary species. This scenario also predicts an almost flat ratio \bar{p}/p in the reacceleration model. Additionally, the index δ_2 of the rigidity dependence of the diffusion coefficient above the break becomes smaller and thus more consistent with CR anisotropy measurements (see a collection of data in Ptuskin et al. 2006a).

The I -scenario implies that the index of the diffusion coefficient has no break. Therefore, the change in the spectral index of secondary species would be the same as that for primaries: $\Delta\epsilon = \Delta\alpha$. The break in the primary and secondary nuclei cancels when we take their ratio as, e.g., the B/C ratio that would be exactly the same if there were no break. In this scenario, the position of the break in the spectra of individual CR species may vary depending on the composition of CR sources injecting particles at low and high energies, while the predicted anisotropy would exceed the actual measurements; see also Malkov et al. (2012).

The local source scenario implies that the local source dominates in some part of the observed spectrum, at low (L -scenario) or high energies (H -scenario). Therefore, the amount of secondaries should drop significantly in the corresponding energy range since the freshly accelerated particles did not have time for fragmentation. A significant contribution of the local source at high energies (H -scenario) would also dramatically increase the CR anisotropy that may be in conflict with observations (Ptuskin et al. 2006a; Sveshnikova et al. 2013).

Vladimirov et al. (2012) concluded that the P -scenario is preferred, but the absence of reliable measurements of secondary species above a few hundred GV at that time did not allow us to distinguish between different options.

Interestingly, soon after that publication, Blasi et al. (2012) proposed a mechanism for the formation of the spectrum of interstellar turbulence. According to this model, the position of the break in the index of the diffusion coefficient corresponds to the case when the diffusive propagation is no longer determined by the self-generated turbulence, but rather by the cascading of externally generated turbulence (for instance, due

to supernova bubbles) from large spatial scales to smaller scales. Independently, on the origin of the break in the spectrum of interstellar turbulence, this would also lead to the expression $\Delta\epsilon = 2\Delta\alpha$. There are other more recent papers that apply various versions of the P -scenario to the available data (e.g., Génolini et al. 2017; Niu et al. 2019).

A subsequent release of the spectra of other primary and secondary species by AMS-02 was eagerly awaited. First, AMS-02 confirmed a clear distinction in the rigidity dependencies between the groups of mostly primary nuclei, He, C, O (Aguilar et al. 2017), and secondary nuclei, Li, Be, B (Aguilar et al. 2018c), while the nuclei within each group have similar spectra. Nitrogen that is half-primary/half-secondary fell in between (Aguilar et al. 2018b). The spectral index of the primary species, C, O, below/above the break is about $\alpha_1/\alpha_2 \approx 2.65/2.55$, while for secondary species it is $\epsilon_1/\epsilon_2 \approx 3.1/2.9$. Here the indices below/above the break were taken at ≈ 50 GV/700 GV, where the solar modulation is negligible. One can see that the change in the spectral index of secondaries $\Delta\epsilon \approx 0.2$ is double the change in the spectral index of primaries $\Delta\alpha \approx 0.1$, as predicted in the P -scenario (Vladimirov et al. 2012) long before the data on secondary species became available (Aguilar et al. 2018c). Note that because there are many different types of sources of CR electrons and positrons and due to the large energy losses of these particles, the spectra of electrons and positrons may behave quite differently and they indeed do so (Aguilar et al. 2019a, 2019b).

3. Numerical Procedure

To derive the LIS of CR species we use the same optimization procedure that was employed in our previous analyses (Boschini et al. 2017, 2018a, 2018b). The combined framework, described in Boschini et al. (2017), is logically divided into two parts: (i) a Markov Chain Monte Carlo (MCMC) interface to version 56 of GALPROP (Masi 2016) that allows for sampling of the production and propagation parameters space, and (ii) an iterative procedure that, starting from GALPROP output, provides modulated spectra computed with HELMOD to compare with AMS-02 data as observational constraints (Boschini et al. 2018c). The final product is a set of Galactic and heliospheric propagation parameters for all CR species to determine the LIS that best reproduces the available experimental data.

The basic properties of CR propagation in the Galaxy are described by the transport equations quite well, but the exact values of the propagation parameters depend on the assumed propagation model and accuracy of selected CR data sets. Therefore, we used the MCMC procedure to determine the propagation parameters using the best available CR data. Five main propagation parameters, which affect the overall shape of CR spectra, were left free in the scan using GALPROP running in the 2D mode: the Galactic halo half-width z_h , the normalization of the diffusion coefficient D_0 at the reference rigidity $R = 4$ GV and the index of its rigidity dependence δ , the Alfvén velocity V_{Alf} , and the gradient of the convection velocity dV_{conv}/dz ($V_{\text{conv}} = 0$ in the plane, $z = 0$). The radial size of the Galaxy does not significantly affect the values of propagation parameters and was set to 20 kpc. Additionally, we introduced a factor β^η in the diffusion coefficient, where $\beta = v/c$, and η was left free. The best-fit value of $\eta = 0.71$

Table 1
Injection Spectra of Primary Species

Isotope	Spectral Parameters			
	$\gamma_0^{R_0(\text{GV})} s_0$	$\gamma_1^{R_1(\text{GV})} s_1$	$\gamma_2^{R_2(\text{GV})} s_2$	γ_3
$^1,^2\text{H}$	2.35 ^{1.15} 0.20	1.71 ^{6.90} 0.23	2.44 ³⁶⁵ 0.09	2.25
$^3,^4\text{He}$	2.24 ^{1.00} 0.20	1.83 ^{7.30} 0.22	2.40 ³²⁵ 0.16	2.15
$^7\text{Li}^a$...	1.10 ^{12.0} 0.16	2.72 ³⁵⁵ 0.13	1.90
$^{12,13}\text{C}$	1.00 ^{0.95} 0.16	2.01 ^{6.10} 0.29	2.42 ³⁴⁰ 0.15	2.12
^{14}N	1.13 ^{1.20} 0.15	1.98 ^{7.00} 0.20	2.44 ³⁰⁰ 0.15	1.87
$^{16,18}\text{O}$	1.11 ^{1.20} 0.19	1.99 ^{7.70} 0.33	2.46 ³⁶⁵ 0.15	2.13
Others	1.12 ^{1.10} 0.16	1.97 ^{7.00} 0.19	2.44 ³⁵⁵ 0.15	2.13

Notes. For definitions of the injection parameters see Equation (1). The fit errors are $\gamma_{0,1} \pm 0.06$, $\gamma_{2,3} \pm 0.04$, $R_0 \pm 0.5$ GV, $R_1 \pm 1$ GV, and $R_2 \pm 15$ GV. In the case of the P -scenario, the parameter γ_3 is not used (see Section 2.3 for details).

^a Models with primary lithium.

improves the agreement at low energies, and slightly affects the choice of injection indices γ_0 and γ_1 (Table 1).

It is worth mentioning that simultaneous inclusion of both distributed reacceleration and convection is necessary to describe the high-precision AMS-02 data, particularly in the range below 10 GV where they significantly affect the spectra of CR species (for more details see Boschini et al. 2017). The best-fit values of the main propagation parameters tuned to AMS-02 data are listed in Table 2, which are about the same as those obtained in Boschini et al. (2017), within the quoted error bars. The most significant change is a slight increase of the Alfvén velocity V_{Alf} that improves agreement with the B/C ratio and electron data (Boschini et al. 2018a).

The MCMC procedure is used only in the first step to define a consistent parameter space, then a methodical calibration of the model employing the HELMOD module was performed. Parameters of the injection spectra, such as spectral indices γ_i and the break rigidities R_i , were also left free, but their exact values depend on the solar modulation, so the low-energy parts of the spectra are tuned together with the solar modulation parameters. The modulated spectra of CR protons are used as a reference for evaluation of the modulation parameters, assuming that all Galactic CRs species are subject to the same heliospheric conditions in the considered energy range. The best-fit injection parameters are listed in Table 1; see also Equation (1) for definitions.

Our calculations of the B/C ratio in the diffusion-convection model are shown in Figures 1 and 2 along with the data by AMS-02 (Aguilar et al. 2018d), PAMELA (Adriani et al. 2014), *High Energy Astrophysics Observatory* (HEAO-3; Engelmann et al. 1990), *Advanced Composition Explorer/Cosmic Ray Isotope Spectrometer* (ACE/CRIS; Lave et al. 2013), and *Voyager* (Cummings et al. 2016). The model and calculations are described in detail in Boschini et al. (2017). The agreement is good for all instruments and all epochs given only one LIS set is inferred from the AMS-02 data.

4. Results

The results of our calculations are compared with available data from AMS-02 (Aguilar et al. 2018b, 2018c), ACE/CRIS (de Nolfo et al. 2006), PAMELA (Adriani et al. 2014), HEAO-3 (Engelmann et al. 1990), and *Voyager* 1 (Cummings et al. 2016). The LIS for pure secondary species, such as beryllium

Table 2
Best-fit Propagation Parameters for I - and P -scenarios

N	Parameter	Units	Best Value	Error
1	z_h	kpc	4.0	0.6
2	D_0 ($R = 4$ GV)	$10^{28} \text{ cm}^2 \text{ s}^{-1}$	4.3	0.7
3 ^a	δ_1		0.415	0.025
4	V_{Alf}	km s^{-1}	30	3
5	dV_{conv}/dz	$\text{km s}^{-1} \text{ kpc}^{-1}$	9.8	0.8

Note.

^a For the P -scenario (see Section 2.3) $\delta_2 = 0.15 \pm 0.03$ for $R \geq 370 \pm 25$ GV.

and boron, were defined assuming LIS spectra for carbon and oxygen as derived in Boschini et al. (2018b) and discussed in the next section. Lithium LIS was initially evaluated using the same procedure. This leads to a large deviation, about 20% excess in the broad range of rigidities from 5 GV–1 TV, when compared to the AMS-02 data: this anomaly is discussed in detail in Section 4.2. In this work we also consider LIS for nitrogen that is approximately half-primary/half-secondary.

4.1. Beryllium, Boron, and Nitrogen

The results of our calculations in the I -scenario, the LIS of beryllium, boron, and nitrogen, are shown in Figures 3–5 and compared to the available data. A comparison of our calculations with data taken at different levels of solar activity and at different polarities of the solar magnetic field demonstrates overall good agreement, thus supporting our model approach.

A moderate overprediction of 10%–20% (at 2–10 GV) is observed in the case of beryllium (Figure 4) when compared to AMS-02 data taken during the same period. Some overprediction ($\sim 20\%$) is also observed when comparing to the *Voyager* 1 (Figure 3) and ACE/CRIS data (Figure 5), but in the latter cases it is at the level of $\lesssim 2\sigma$. The overprediction in beryllium flux below a few GV is most likely connected with errors in the total inelastic cross sections of beryllium isotopes. The cross-section errors are most significant in the case of beryllium, and in particular, in the energy range below 10 GeV/n (see Figure 6 in Génolini et al. 2018).

Other discrepancies, such as those reported in Figure 5 for beryllium, boron, and nitrogen when comparing to the HEAO-3 data (Engelmann et al. 1990), are an indication of the systematic uncertainties of the instrument. This is demonstrated by the excellent agreement of spectra of boron and nitrogen with AMS-02 data (Aguilar et al. 2018c) in the whole energy range from 2 GV–2 TV.

Our results for the I - and P -scenarios are shown in Figures 6–8. Since the spectral behavior of CR nuclei at low energies is the same in both scenarios (also in plots in our earlier papers Boschini et al. 2017, 2018b), the P -scenario calculations are only shown above ~ 100 GV, where the effects of solar modulation can be safely neglected. Figure 6 shows the B/C ratio in the P -scenario together with AMS-02 data taken at different epochs. The flattening above ~ 350 GV is clearly seen, but it is very moderate and agrees well with data.

The spectra of all nuclei species, Be, B, C, N, O, calculated in both scenarios, are shown in Figures 7 and 8. In both cases the agreement with data is good. In the case of the P -scenario we use only the parameters $\gamma_{0,1,2}$ and $R_{0,1}$ from Table 1, while

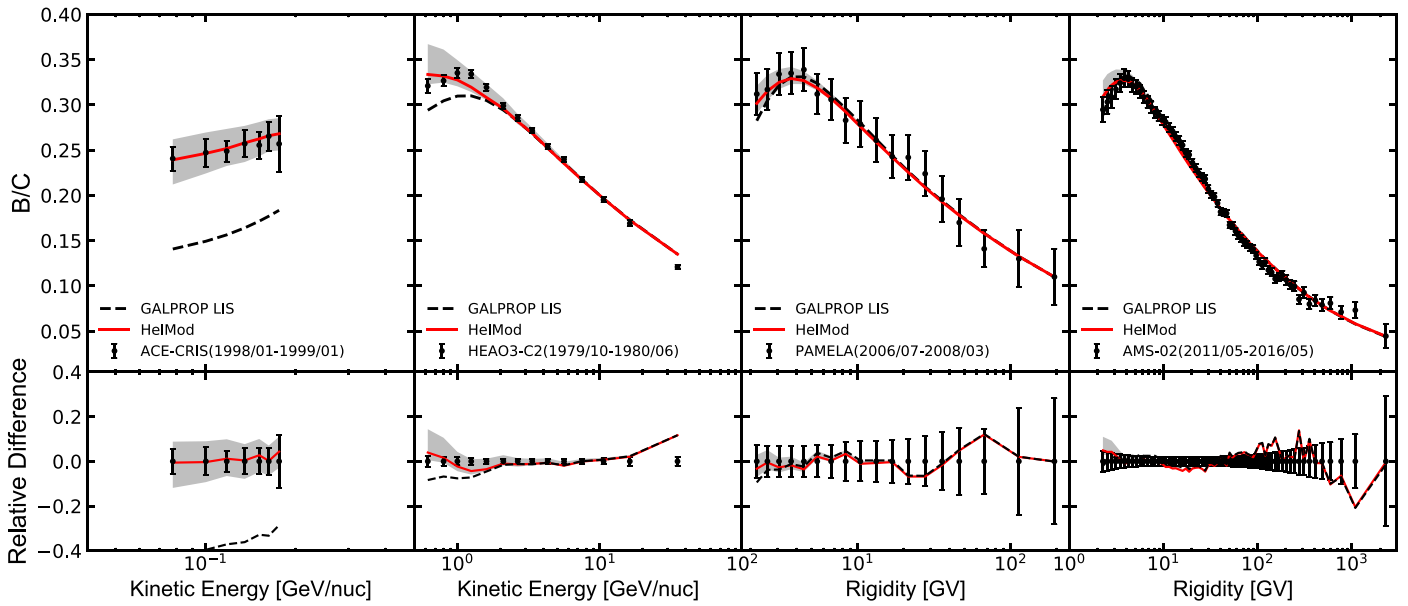


Figure 1. Top panels: the B/C ratio as measured by (from left to right) *ACE/CRIS* (Lave et al. 2013), *HEAO-3* (Engelmann et al. 1990), *PAMELA* (Adriani et al. 2014), and *AMS-02* (Aguilar et al. 2018d) compared to our calculations. The dashed black line shows the GALPROP LIS ratio (*L*-scenario), and the modulated ratios (that correspond to each individual period of data taking) are shown by the red lines. Bottom panels: relative difference between the calculations and a corresponding experimental data set.

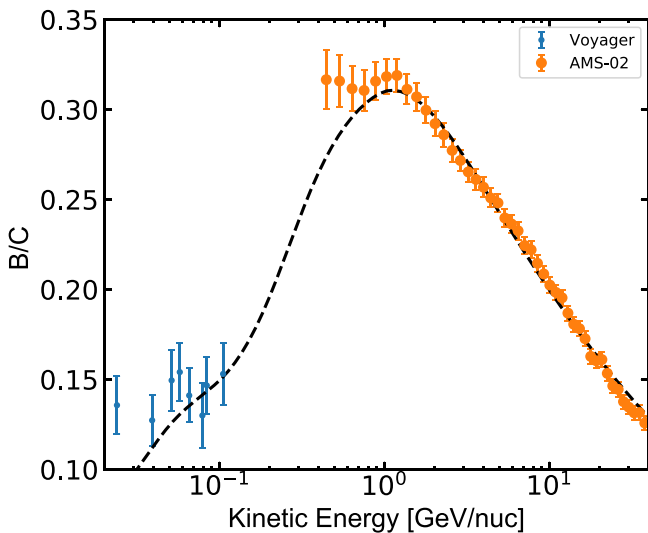


Figure 2. The B/C ratio as measured by *AMS-02* (Aguilar et al. 2018d) and by *Voyager 1* (Cummings et al. 2016) reported in units of kinetic energy per nucleon. The dashed black line shows the GALPROP LIS ratio. *AMS-02* data in kinetic energy per nucleon are those obtained from the Italian Space Agency (ASI) Cosmic Ray Database (Di Felice et al. 2017).

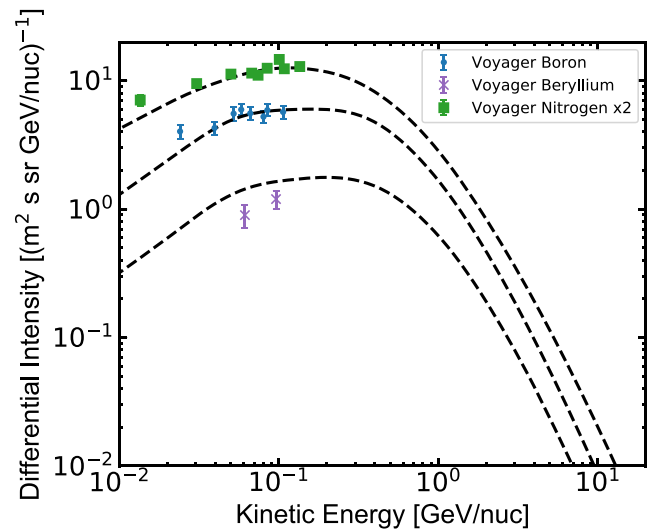


Figure 3. GALPROP LIS spectra (black dashed lines) compared to the *Voyager 1* data (Cummings et al. 2016): boron: small blue dots; beryllium: violet crosses; and nitrogen: green squares. The nitrogen spectrum is scaled up by a factor of 2 for clarity.

4.2. Lithium Anomaly

the break at ~ 350 GV appears due to the break in the diffusion coefficient (Table 2).

The effect of the local source producing low-energy CRs (*L*-scenario) on the observed composition of CRs and production of secondaries was studied in Moskalenko et al. (2003) and Vladimirov et al. (2012). In short, tuning to the observed secondary-to-primary ratio, such as B/C, would require a significant decrease in the normalization of the diffusion coefficient in order to compensate for the presence of locally produced primary species, such as C and O. This, in turn, would lead to an increase of the \bar{p}/p ratio. However, a detailed exploration of this scenario is beyond the scope of this work.

A demonstrated good agreement of our model calculations with measurements of CR species in a wide energy range implies that lithium spectrum should also be well reproduced by the same model. However, a comparison of our calculations of secondary lithium with data exhibits a significant excess over the model predictions above a few GV (Figures 9 and 10) even though the propagation parameters are tuned to the B/C ratio. The additional *secondary* ${}^7\text{Li}$ cannot come from the decay of ${}^7\text{Be}$ isotope in CRs that decay via K-capture. All GALPROP calculations are already run with the processes of electron pickup, stripping, and K-capture included. Therefore, this may indicate that some part of the observed lithium has a different origin.

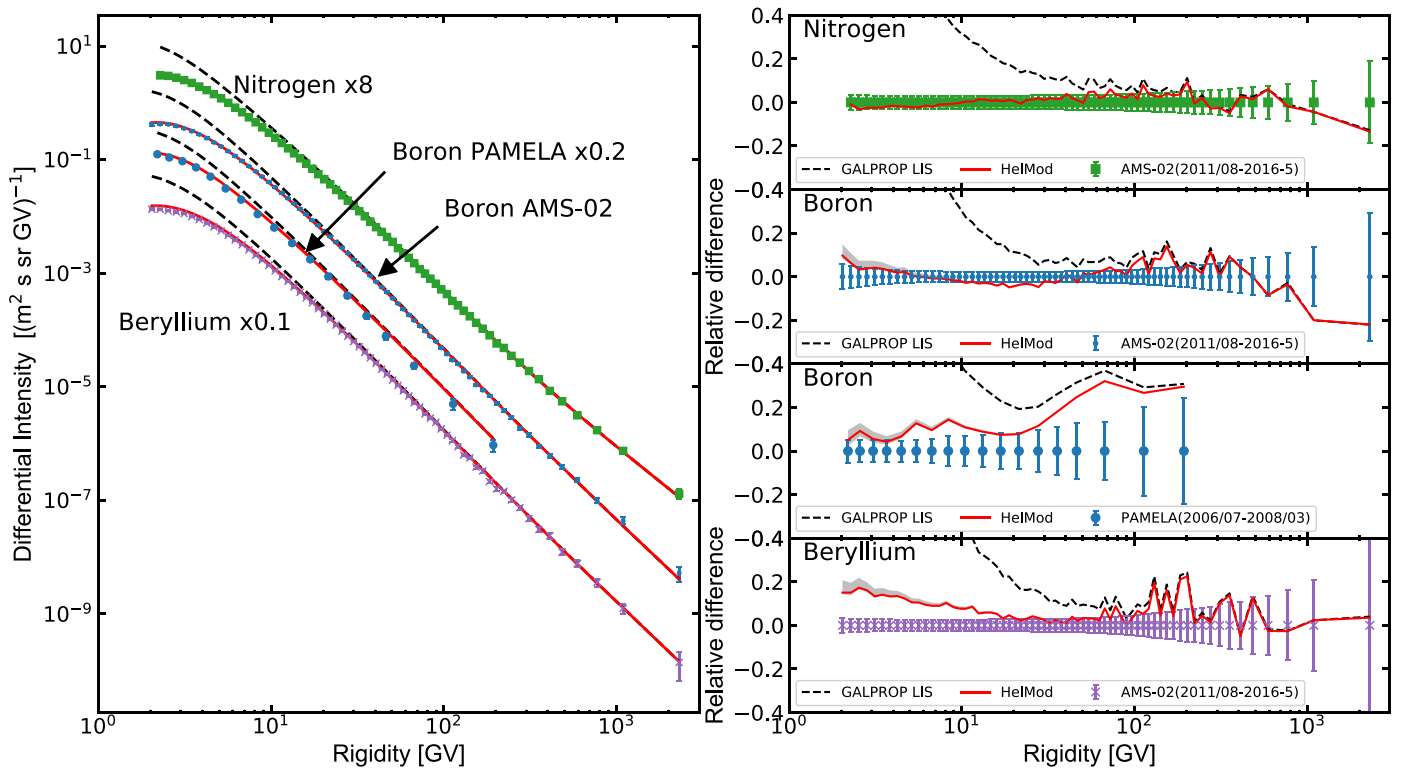


Figure 4. Our model calculations compared to the observed CR spectra of nitrogen (green squares), boron (blue dots), and beryllium (violet crosses) from AMS-02 (Aguilar et al. 2018b, 2018c) and PAMELA (boron: filled blue circles, Adriani et al. 2014). The black dashed line shows the LIS spectra (L -scenario), and the red solid lines are modulated to the level that corresponds to the period of data taking. For clarity, the AMS-02 spectra of nitrogen and beryllium, and the PAMELA spectrum of boron are scaled by factors 8, 0.1, and 0.2, respectively. The right panel show the relative difference between calculations and a corresponding experimental data set.

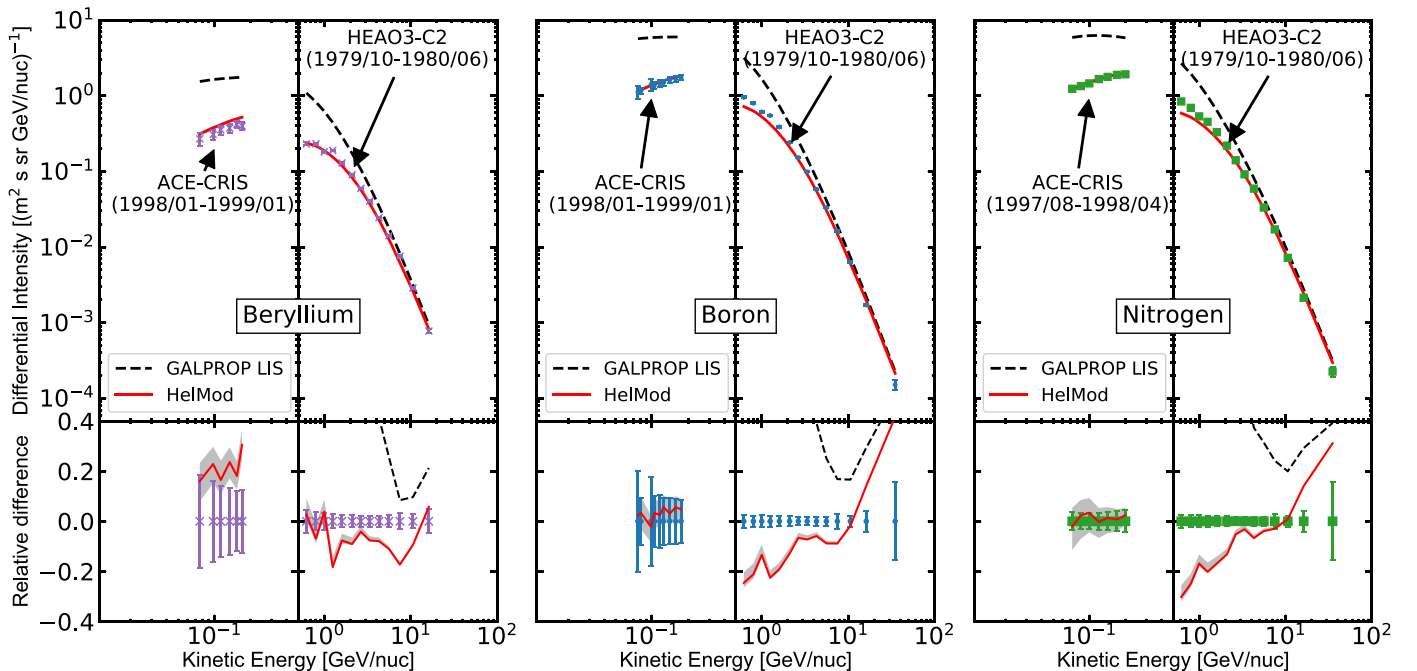


Figure 5. Our model calculations compared to the observed CR spectra of beryllium (violet crosses, left panel), boron (blue points, center panel), and nitrogen (green squares, right panel) from ACE-CRIS (de Nolfo et al. 2006) and HEAO3-C2 (Engelmann et al. 1990). The black dashed lines show the LIS spectra, and the red solid lines are modulated to the levels that correspond to the periods of data taking. Bottom panels: relative difference between the calculations and a corresponding experimental data set.

Meanwhile, a possibly connected puzzle is a long-standing problem of the origin of lithium observed in today's universe (e.g., Hernanz 2015). While some fraction of lithium was created in the primordial nucleosynthesis, most of the observed

lithium is produced through interactions of energetic CR particles with interstellar gas (spallation reactions). On the other hand, the observed stellar lithium abundances indicate that some proportion of lithium is also produced in low-mass

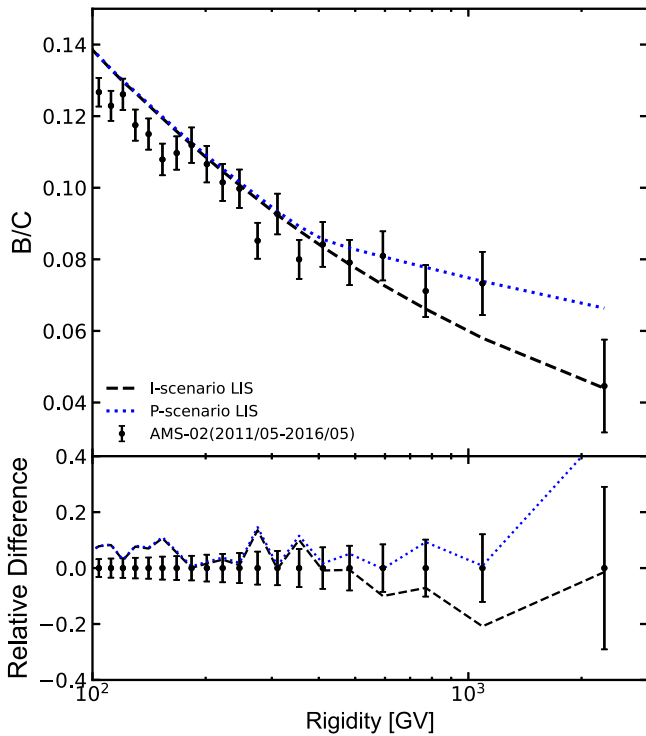


Figure 6. Our model calculations of the B/C ratio in the *I*-scenario (dashed black line) and *P*-scenario (blue dotted line) compared to the AMS-02 data (Aguilar et al. 2018d). Bottom panel: relative difference between the calculations and a corresponding experimental data set.

stars and nova explosions. Indeed, the alpha-capture reaction of ${}^7\text{Be}$ production ${}^3\text{He}(\alpha, \gamma){}^7\text{Be}$ was proposed a while ago (Cameron 1955; Cameron & Fowler 1971). A subsequent decay of ${}^7\text{Be}$ with a half-life of 53.22 days yields ${}^7\text{Li}$ isotope. To ensure that produced ${}^7\text{Li}$ is not destroyed in subsequent nuclear reactions, ${}^7\text{Be}$ should be transported into cooler layers where it can decay to ${}^7\text{Li}$, the so-called Cameron–Fowler mechanism.

The production of ${}^7\text{Li}$ in the same reactions in novae was first discussed by Arnould & Norgaard (1975) and Starrfield et al. (1978), while the details of the process were established later (Hernanz et al. 1996). The amount of ${}^7\text{Li}$ produced by a classical CO nova corresponds to about $10^{-10}M_{\odot}$ – $10^{-9}M_{\odot}$, although the exact amount depends on many details of the explosion process.

Recent observation of blueshifted absorption lines of partly ionized ${}^7\text{Be}$ in the spectrum of a classical nova V339 Del about 40–50 days after the explosion (Tajitsu et al. 2015) is the first observational evidence that the mechanism proposed in 1970s is working indeed (Hernanz 2015). The observed blueshift of the absorption lines corresponds to the velocity of the ejecta reaching 1100–1270 km s $^{-1}$. Consequent observations of other novae (V1369 Cen, Izzo et al. 2015; V5668 Sgr and V2944 Oph, Tajitsu et al. 2016; ASASSN-16kt [V407 Lupi], Izzo et al. 2018; V838 Her, Selvelli et al. 2018) also reveal the presence of ${}^7\text{Be}$ lines in their spectra, indicating that classical novae are the new type of sources of ${}^7\text{Li}$. The total mass of produced ${}^7\text{Li}$ in these novae is estimated from $10^{-9}M_{\odot}$ – $6 \times 10^{-9}M_{\odot}$.

For our case this means that there is a source of primary lithium and that this lithium may be observed in CRs for the first time, thanks to the high statistics and precision achieved by the AMS-02 experiment (Aguilar et al. 2018c). Though the absolute mass of lithium produced by novae is relatively small, the

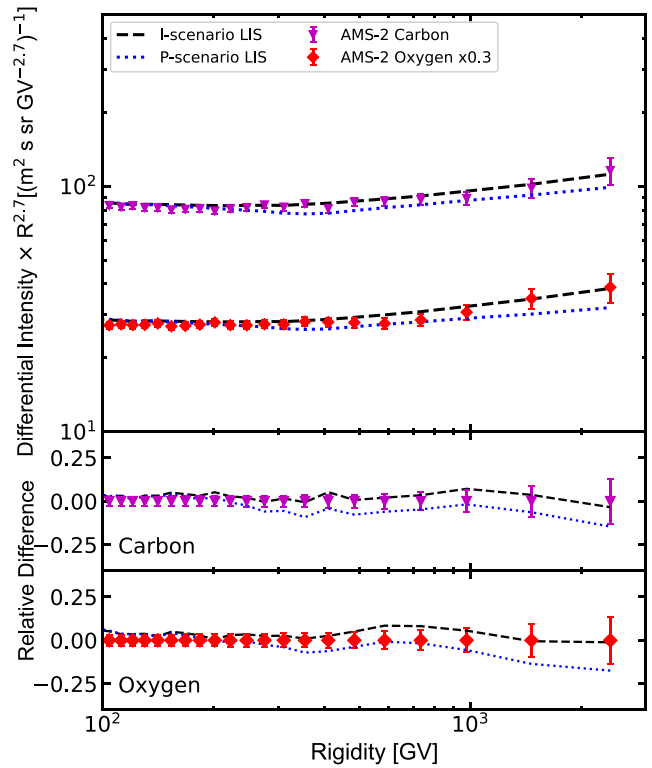


Figure 7. Our model calculations of the carbon and oxygen spectra in the *I*-scenario (dashed black line) and *P*-scenario (blue dotted line) compared to the AMS-02 data (Aguilar et al. 2017). The experimental data points for carbon are shown by violet triangles, and those for oxygen are shown by red diamonds. The differential intensity is multiplied by $R^{2.7}$ to enhance the high-energy differences. The oxygen spectrum is scaled by a factor of 0.3 for clarity. The bottom panels show the relative difference between the calculations and a corresponding experimental data set.

lithium abundance of the ejecta is comparable to that found in CRs given that the total mass of the ejecta is $10^{-5}M_{\odot}$ – $10^{-4}M_{\odot}$. Such lithium-enriched ejecta could serve as a source of primary lithium that is subsequently accelerated in nova and SN shocks, thus supplying additional lithium to CRs.

We note that a similar mechanism was proposed by Kawanaka & Yanagita (2018) albeit with the rather extreme assumption that the spectral hardening observed above 300 GV is due to the local SN Ia. In this model most of the protons, He, and lithium above the break are coming from the local source. This is equivalent to the *H*-scenario originally considered in Vladimirov et al. (2012) and deemed unlikely, since it would lead to a dramatic increase in CR anisotropy at very high energies, contrary to the observations, and a sharp drop in the B/C ratio above the break that is not observed either (see also a discussion in Section 2.3).

Figure 10 shows a fit (*I*-scenario) where a small amount of primary ${}^7\text{Li}$ was injected with parameters given in Table 1, in addition to the secondary lithium. The agreement with the AMS-02 data (Aguilar et al. 2018c) is significantly improved. A small discrepancy around 2 GV is still remaining that may indicate some unknown systematics. A calculation in the *P*-scenario looks similar and is not shown in this plot.

Our calculations of the lithium spectrum in the *P*-scenario shown in Figure 8 already contain primary ${}^7\text{Li}$ that improves the agreement significantly. In this scenario, the injection spectrum of primary ${}^7\text{Li}$ is the same as that in the case of the *I*-scenario (Table 1), but the parameter γ_3 is not used. This calculation

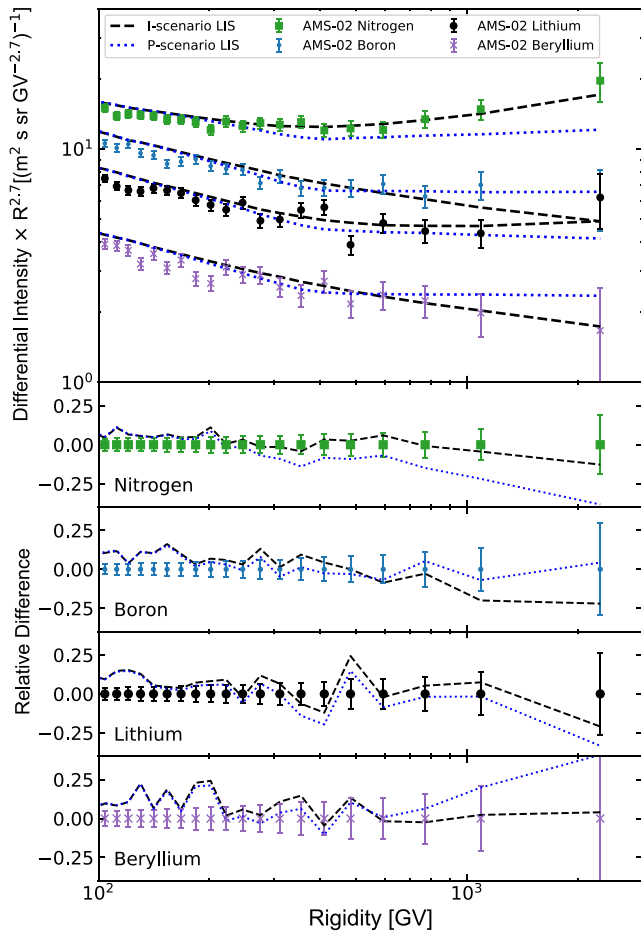


Figure 8. Our model calculations of the nitrogen, boron, lithium, and beryllium spectra in the *I*-scenario (dashed black line) and *P*-scenario (blue dotted line) compared to the AMS-02 data (Aguilar et al. 2018d). The experimental data points are: nitrogen: green squares; boron: blue points; lithium: black filled circles; and beryllium: violet crosses. The differential intensity is multiplied by $R^{2.7}$ to enhance the high-energy differences. Bottom panels: relative difference between the calculations and a corresponding experimental data set.

illustrates that the *P*-scenario is consistent with all data available from AMS-02 and earlier experiments and seems like a natural explanation of the break in the spectra of all CR nuclei species observed at ~ 350 GV. Note that the *I*-scenario provides a similar quality fit, but at the cost of additional parameters.

Another possible reason for this discrepancy is that the lithium production cross sections that we employ in our propagation code are incorrect. However, from the compilation of the production cross sections (Génolini et al. 2018), one can see that the major production channels are fragmentation of carbon and oxygen, $^{12}\text{C}, ^{16}\text{O} + p \rightarrow ^{6,7}\text{Li}$, that have been each measured in several different experiments. Even though they are not measured perfectly, each of them is contributing 12%–14% and thus a 20% error in one of them would correspond to only 2%–3% of total lithium production. Other production channels are contributing at a level of 1%–2% or less. It is not impossible, but rather unlikely that cross-section errors are all biased on the same side leading to the observed 20% excess.

Finally, one can see that the AMS-02 lithium data show a kink around ~ 100 GV (Figure 10), while the error bars there are rather small. Such irregularity and the relatively large scattering of data points above this rigidity may be partially responsible for the excessive hardening of the lithium spectrum

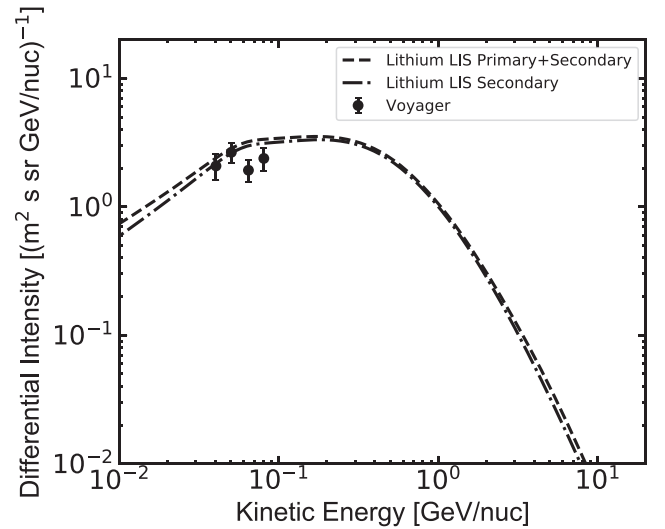


Figure 9. Our calculated spectra of secondary lithium (dotted–dashed line) and lithium with an added primary ^7Li component (dashed line) compared to the Voyager 1 data (Cummings et al. 2016).

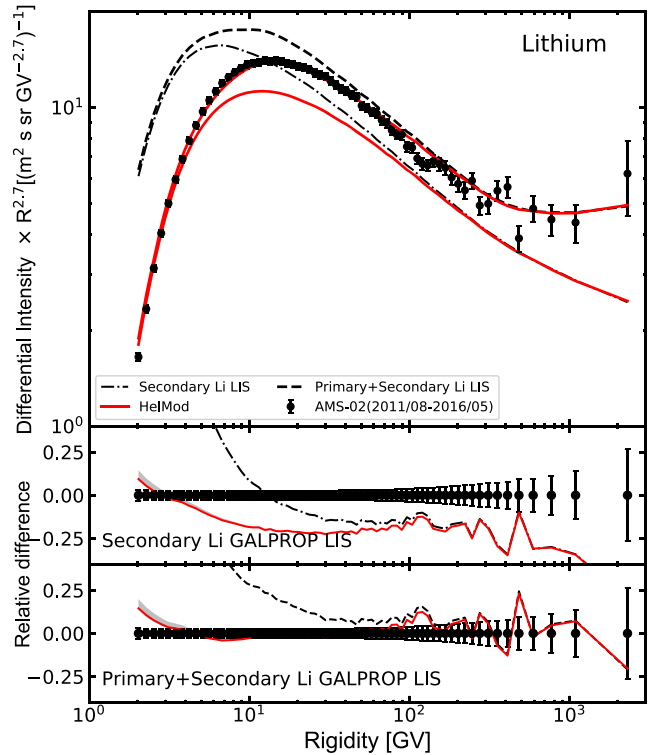


Figure 10. Our model calculations of CR lithium (in the *I*-scenario) compared to the AMS-02 data (Aguilar et al. 2018c). The black dotted–dashed line shows only the secondary component. The black dashed line shows the calculations that include the primary ^7Li component. The red solid lines are modulated to the level that corresponds to the period of data taking. In the top panel, the differential intensity is multiplied by $R^{2.7}$ to enhance high-energy differences.

above ~ 100 GV. Here we have to wait for further data releases, which should indicate if this kink is an instrumental artifact or a real spectral feature and also improve the statistics at high energies. Meanwhile, since the lithium excess is present even at lower energies, $\gtrsim 4$ GV, we believe that the effect is real, though the fitted values may change somewhat when the more accurate data become available.

The ultimate test of the origin of lithium in CRs would be a measurement of its isotopic composition at high energies. The nova origin of primary ${}^7\text{Li}$ would lead to the dominance of ${}^7\text{Li}$ at high energies, while at low energies the abundances of ${}^6\text{Li}$ and ${}^7\text{Li}$ are about the same. However, isotopic abundances are very difficult to measure at high energies and would require a large magnetic spectrometer with a superconducting magnet in space. The outlines of such future instruments are currently discussed in the literature (Schael et al. 2019), but building and launching them into space may take a couple of decades. We therefore should concentrate on elimination of other possibilities through new measurements of the production cross sections or reevaluation of the available data.

5. Discussion

It is relevant to illustrate reasons for the apparent discrepancies between the propagation parameters derived in our present analysis and the earlier Bayesian analysis (Jóhannesson et al. 2016, hereafter paper J2016) of propagation of two independent sets of CR species, \bar{p} , p , He (hereafter \bar{p} set), on the one hand, and Be to O nuclei (hereafter Be-O set), on the other hand, that was also based on GALPROP. In short, the two sets of data (\bar{p} set and Be-O set) taken separately yield normalizations of the diffusion coefficient and the Alfvén velocities, which are inconsistent with each other (see a plot V_{Alf} versus D_0 in Figure 3 in J2016), suggesting that properties of the interstellar medium in the Galaxy differ on different scales. The latter follows from a comparison of the *effective* propagation distances of these species that are significantly different due to differences in the total inelastic cross sections (~ 40 mb for p and \bar{p} versus ~ 250 mb for carbon). This conclusion is somewhat contradictory to the conclusion made in the current series of our papers (Boschini et al. 2017, 2018a, 2018b, and the present paper, hereafter *B-series* papers) that the same propagation parameters can be used to describe the propagation of all light CR species, including \bar{p} and H-O nuclei.

While the properties of the interstellar medium can vary on different scales indeed, and to definitively test it, we have to wait for accurate measurements of heavier CR species with larger fragmentation cross sections, preferably such as Fe and heavier, we shall discuss here what makes the conclusions from the two analyses somewhat different. We can see at least three major areas that can lead to some differences in the results: (i) the approach, (ii) the sets of data used, and (iii) the treatment of the heliospheric propagation. Here we discuss them one by one.

(i) In the *B-series* papers, in each case the propagation parameters are derived using the B/C ratio assuming a *diffusion-convection-reacceleration* model. In Boschini et al. (2017) no attempt to fit the CR \bar{p} spectrum was made; instead the \bar{p} spectrum was calculated using the set of propagation parameters derived from the B/C ratio and fits to the spectra of protons and helium. Additionally, the \bar{p} production cross sections used in the *B-series* are tuned to the modern accelerator data using the Monte Carlo event generator QGSJET-II-04 m (Kachelriess et al. 2015, 2019). In contrast, in J2016, the \bar{p} set of propagation parameters was tuned to the CR p , He, and \bar{p} spectra in the *diffusion-reacceleration* model *excluding* all other CR species, while \bar{p} production was calculated using considerably older cross-section parameterizations (Tan & Ng 1983a, 1983b; Moskalenko et al. 2002).

(ii) The current analysis (*B-series*) uses precise AMS-02 data for all light species, such as \bar{p} , and H-O nuclei, which were not

available at the time when the Bayesian analysis was ran, thus the J2016 paper used mostly the *ACE/CRIS*, *HEAO-3*, and *PAMELA* data. Meanwhile, there are significant systematic discrepancies between different instruments (AMS-02 versus *HEAO-3* and *PAMELA*) even at the energies where the effect of the solar modulation is small; see examples in Figures 4 and 5. The CR \bar{p} data also became significantly more accurate (see Figure 13 in Boschini et al. 2017).

(iii) The treatment of the solar modulation became exceedingly more precise. In the *B-series* we use the sophisticated *HelMod* code, which includes the complete treatment of solar modulation mechanisms and is tuned to the data of numerous spacecraft taken at different levels of solar activity and polarities of the solar magnetic field, including measurements at different heliospheric distances (e.g., *Voyager 1, 2*, *Pioneer 10, 11*) and outside of the ecliptic plane (*Ulysses*); see Section 2.2 for more details. Meanwhile, the calculations J2016 used rather simplified the force-field approximation with a single parameter. To accommodate the unknown systematic uncertainties of different instruments to a priori unknown levels of the solar modulation, a total of eight nuisance and rescaling parameters were used. Meanwhile, a proper treatment of the heliospheric propagation in J2016 would be unfeasible given the already heavy computation load.

Nevertheless, the parameters derived in J2016 for the Be-O set look quite consistent with those derived in the current *B-series*. The posterior normalizations of the diffusion coefficient in the two sets of data are $D_0 = 6.102 \pm 1.662$ (\bar{p} set) and 9.030 ± 1.610 (Be-O set) in units of $10^{28} \text{ cm}^2 \text{ s}^{-1}$ (Table 4 in J2016) versus 4.3 ± 0.7 (this paper, Table 2) in the same units and at the same normalization rigidity. The former two values look quite reasonable given that the posterior halo sizes are considerably larger in J2016, $z_h = 10.358 \pm 4.861$ kpc (\bar{p} set) and 10.351 ± 4.202 kpc (Be-O set) versus 4.0 ± 0.6 kpc in this paper, so the ratios $D_0/z_h \approx 0.9 \pm 0.5$ (Be-O set, J2016) and $D_0/z_h \approx 1.1 \pm 0.3$ (*B-series*) in units of $10^{28} \text{ cm}^2 \text{ s}^{-1} \text{ kpc}^{-1}$ are consistent.¹³ In the case of the \bar{p} set (J2016), $D_0/z_h \approx 0.6 \pm 0.4$ in the same units, i.e., it is still consistent with other ratios. Additionally, the (J2016) calculations do not include the convection, which implies some intrinsic difference with the present analysis.

The indices of the rigidity dependence of the diffusion coefficient are also consistent, 0.461 ± 0.065 (\bar{p} set) and 0.380 ± 0.018 (Be-O set) versus 0.415 ± 0.025 in this paper, so as the Alfvén velocity derived for the Be-O set, $V_{\text{Alf}} = 30.017 \pm 2.461 \text{ km s}^{-1}$ versus $30 \pm 3 \text{ km s}^{-1}$ (*B-series*). The significant deviation is a relatively small Alfvén velocity, $8.970 \pm 1.244 \text{ km s}^{-1}$, derived for the \bar{p} set. An obvious explanation of this difference is that due to the characteristic shape of the CR \bar{p} spectrum that is suppressed at low energies, the fit prefers a weak reacceleration (see also Moskalenko et al. 2002). If a new fit to the \bar{p} data is attempted, it would likely yield values similar to those obtained for the \bar{p} set in J2016. Meanwhile, for a correct interpretation of the fit results, the accuracy of the used \bar{p} production cross sections should be comparable to or exceed the accuracy of the CR data, and new accelerator measurements of the \bar{p} production in the whole relevant energy range would be very valuable here.

In any case, it is important to repeat such types of analyses when accurate data for heavier nuclei become available in order

¹³ Note that the ratio D_0/z_h is an approximate invariant for a given propagation model (for more details see, e.g., Berezhinskii et al. 1990; Strong et al. 2007).

Table 3
Lithium LIS

Rigidity GV	Differential Intensity ^a	Rigidity GV	Differential Intensity ^a	Rigidity GV	Differential Intensity ^a	Rigidity GV	Differential Intensity ^a	Rigidity GV	Differential Intensity ^a
1.007e-01	3.173e-03	6.359e-01	3.767e-01	5.303e+00	1.837e-01	1.552e+02	8.331e-06	5.976e+03	3.570e-10
1.057e-01	3.634e-03	6.680e-01	4.209e-01	5.691e+00	1.541e-01	1.706e+02	6.196e-06	6.581e+03	2.802e-10
1.109e-01	4.106e-03	7.018e-01	4.656e-01	6.113e+00	1.285e-01	1.877e+02	4.608e-06	7.247e+03	2.201e-10
1.164e-01	4.638e-03	7.374e-01	5.088e-01	6.575e+00	1.065e-01	2.065e+02	3.429e-06	7.981e+03	1.730e-10
1.222e-01	5.241e-03	7.749e-01	5.489e-01	7.080e+00	8.777e-02	2.272e+02	2.553e-06	8.789e+03	1.361e-10
1.282e-01	5.923e-03	8.144e-01	5.856e-01	7.633e+00	7.201e-02	2.500e+02	1.903e-06	9.678e+03	1.071e-10
1.346e-01	6.695e-03	8.561e-01	6.181e-01	8.238e+00	5.881e-02	2.751e+02	1.421e-06	1.066e+04	8.438e-11
1.412e-01	7.569e-03	9.000e-01	6.481e-01	8.900e+00	4.784e-02	3.027e+02	1.063e-06	1.174e+04	6.651e-11
1.482e-01	8.559e-03	9.463e-01	6.776e-01	9.627e+00	3.875e-02	3.331e+02	7.976e-07	1.293e+04	5.245e-11
1.555e-01	9.681e-03	9.953e-01	7.088e-01	1.042e+01	3.124e-02	3.666e+02	6.007e-07	1.423e+04	4.139e-11
1.632e-01	1.095e-02	1.047e+00	7.434e-01	1.130e+01	2.505e-02	4.035e+02	4.542e-07	1.567e+04	3.268e-11
1.713e-01	1.239e-02	1.102e+00	7.795e-01	1.226e+01	1.996e-02	4.442e+02	3.447e-07	1.726e+04	2.582e-11
1.798e-01	1.402e-02	1.159e+00	8.161e-01	1.332e+01	1.579e-02	4.889e+02	2.624e-07	1.901e+04	2.041e-11
1.887e-01	1.587e-02	1.220e+00	8.517e-01	1.448e+01	1.241e-02	5.382e+02	2.004e-07	2.093e+04	1.614e-11
1.980e-01	1.797e-02	1.285e+00	8.850e-01	1.575e+01	9.691e-03	5.925e+02	1.534e-07	2.305e+04	1.278e-11
2.078e-01	2.035e-02	1.354e+00	9.151e-01	1.715e+01	7.525e-03	6.522e+02	1.176e-07	2.539e+04	1.011e-11
2.181e-01	2.304e-02	1.427e+00	9.407e-01	1.869e+01	5.814e-03	7.180e+02	9.035e-08	2.796e+04	8.012e-12
2.289e-01	2.610e-02	1.504e+00	9.608e-01	2.039e+01	4.473e-03	7.905e+02	6.951e-08	3.079e+04	6.349e-12
2.403e-01	2.957e-02	1.586e+00	9.745e-01	2.226e+01	3.428e-03	8.703e+02	5.355e-08	3.390e+04	5.034e-12
2.522e-01	3.351e-02	1.673e+00	9.810e-01	2.431e+01	2.619e-03	9.582e+02	4.131e-08	3.733e+04	3.993e-12
2.647e-01	3.799e-02	1.766e+00	9.795e-01	2.657e+01	1.996e-03	1.055e+03	3.190e-08	4.111e+04	3.168e-12
2.778e-01	4.307e-02	1.865e+00	9.695e-01	2.905e+01	1.517e-03	1.162e+03	2.466e-08	4.528e+04	2.515e-12
2.916e-01	4.886e-02	1.971e+00	9.508e-01	3.179e+01	1.150e-03	1.279e+03	1.909e-08	4.986e+04	1.997e-12
3.061e-01	5.544e-02	2.084e+00	9.236e-01	3.480e+01	8.701e-04	1.408e+03	1.479e-08	5.491e+04	1.587e-12
3.213e-01	6.293e-02	2.204e+00	8.881e-01	3.812e+01	6.571e-04	1.551e+03	1.147e-08	6.047e+04	1.261e-12
3.372e-01	7.147e-02	2.334e+00	8.453e-01	4.177e+01	4.953e-04	1.707e+03	8.906e-09	6.659e+04	1.002e-12
3.540e-01	8.121e-02	2.472e+00	7.959e-01	4.579e+01	3.727e-04	1.880e+03	6.919e-09	7.333e+04	7.972e-13
3.716e-01	9.233e-02	2.621e+00	7.414e-01	5.022e+01	2.800e-04	2.070e+03	5.380e-09	8.076e+04	6.341e-13
3.901e-01	1.050e-01	2.781e+00	6.837e-01	5.509e+01	2.100e-04	2.280e+03	4.187e-09	8.893e+04	5.046e-13
4.096e-01	1.196e-01	2.954e+00	6.243e-01	6.046e+01	1.573e-04	2.510e+03	3.261e-09	9.794e+04	4.016e-13
4.300e-01	1.363e-01	3.139e+00	5.645e-01	6.637e+01	1.177e-04	2.764e+03	2.543e-09	1.079e+05	3.197e-13
4.514e-01	1.554e-01	3.340e+00	5.060e-01	7.287e+01	8.793e-05	3.044e+03	1.984e-09	1.188e+05	2.546e-13
4.740e-01	1.771e-01	3.557e+00	4.495e-01	8.004e+01	6.565e-05	3.352e+03	1.549e-09	1.308e+05	2.028e-13
4.977e-01	2.017e-01	3.791e+00	3.956e-01	8.792e+01	4.897e-05	3.691e+03	1.211e-09	1.440e+05	1.616e-13
5.226e-01	2.295e-01	4.046e+00	3.451e-01	9.661e+01	3.650e-05	4.064e+03	9.470e-10	1.586e+05	1.287e-13
5.488e-01	2.609e-01	4.322e+00	2.983e-01	1.062e+02	2.719e-05	4.476e+03	7.412e-10	1.747e+05	1.026e-13
5.764e-01	2.961e-01	4.622e+00	2.558e-01	1.167e+02	2.024e-05	4.928e+03	5.806e-10	1.924e+05	8.176e-14
6.054e-01	3.349e-01	4.948e+00	2.176e-01	1.283e+02	1.506e-05	5.427e+03	4.551e-10	2.118e+05	6.486e-14

Note.^a Differential intensity units: (m² s sr GV)⁻¹.

(This table is available in its entirety in machine-readable form.)

to see if the propagation parameters derived from fits to different CR species are consistent or systematically different.

6. Conclusion

The paper presents our results for the analysis of the Galactic propagation and heliospheric transport of the secondary species, lithium, beryllium, boron, and nitrogen, which have a considerable secondary contribution. The derived LIS allow a consistent reproduction of all available data from different instruments, while also indicating likely considerable instrumental systematic uncertainties (e.g., *HEAO-3* versus *AMS-02*). In the [Appendix](#) we provide analytical fits to the calculated LIS of lithium, beryllium, boron, and nitrogen for the energy range from 350 MV–50 TV, Equations (5)–(8), as well as fully numerical output tables of the LIS from GALPROP runs, Tables 3–6. The fits are tuned to match the GALPROP-calculated LIS within 1%–5% over five orders of magnitude in

rigidity, including the spectral flattening at high energies. The numerical values in the fits and tables correspond to the *I*-scenario, which has more free parameters, therefore the fits to the data are more accurate; see Figures 7 and 8. The search for the analytical expressions of the fit functions—using the same algorithm as described in [Boschini et al. \(2017\)](#)—was guided by the advanced MCMC fitting procedure *Eureqa*.¹⁴

Contrary to the mostly primary species, whose injection spectra could be adjusted to match the observations and thus hide the model uncertainties associated with the cross sections, assumed source and gas distributions, and other input parameters, the secondary species are not that forgiving. Instead, in the case of secondary nuclei, all errors associated with the description of the propagation of primary species are popping

¹⁴ <http://www.nutonian.com/products/eureqa/>

Table 4
Beryllium LIS

Rigidity GV	Differential Intensity ^a	Rigidity GV	Differential Intensity ^a	Rigidity GV	Differential Intensity ^a	Rigidity GV	Differential Intensity ^a	Rigidity GV	Differential Intensity ^a
7.555e-02	6.565e-04	4.769e-01	1.412e-01	3.977e+00	1.889e-01	1.164e+02	1.078e-05	4.482e+03	2.078e-10
7.929e-02	8.939e-04	5.010e-01	1.581e-01	4.268e+00	1.624e-01	1.280e+02	8.021e-06	4.936e+03	1.570e-10
8.321e-02	1.116e-03	5.264e-01	1.759e-01	4.585e+00	1.383e-01	1.408e+02	5.968e-06	5.436e+03	1.186e-10
8.732e-02	1.340e-03	5.531e-01	1.944e-01	4.931e+00	1.167e-01	1.549e+02	4.440e-06	5.986e+03	8.959e-11
9.164e-02	1.570e-03	5.812e-01	2.138e-01	5.310e+00	9.759e-02	1.704e+02	3.303e-06	6.592e+03	6.767e-11
9.617e-02	1.812e-03	6.108e-01	2.340e-01	5.724e+00	8.101e-02	1.875e+02	2.458e-06	7.259e+03	5.111e-11
1.009e-01	2.073e-03	6.421e-01	2.551e-01	6.178e+00	6.673e-02	2.063e+02	1.830e-06	7.994e+03	3.859e-11
1.059e-01	2.361e-03	6.750e-01	2.768e-01	6.675e+00	5.458e-02	2.270e+02	1.363e-06	8.803e+03	2.914e-11
1.112e-01	2.688e-03	7.098e-01	2.991e-01	7.220e+00	4.437e-02	2.498e+02	1.016e-06	9.694e+03	2.200e-11
1.167e-01	3.062e-03	7.465e-01	3.213e-01	7.818e+00	3.585e-02	2.750e+02	7.576e-07	1.068e+04	1.661e-11
1.224e-01	3.487e-03	7.852e-01	3.429e-01	8.475e+00	2.878e-02	3.026e+02	5.657e-07	1.176e+04	1.254e-11
1.285e-01	3.972e-03	8.262e-01	3.637e-01	9.195e+00	2.294e-02	3.331e+02	4.228e-07	1.295e+04	9.466e-12
1.348e-01	4.526e-03	8.695e-01	3.843e-01	9.987e+00	1.821e-02	3.667e+02	3.163e-07	1.426e+04	7.145e-12
1.415e-01	5.158e-03	9.153e-01	4.049e-01	1.086e+01	1.436e-02	4.036e+02	2.370e-07	1.570e+04	5.393e-12
1.485e-01	5.879e-03	9.639e-01	4.252e-01	1.181e+01	1.125e-02	4.443e+02	1.777e-07	1.729e+04	4.070e-12
1.559e-01	6.702e-03	1.015e+00	4.452e-01	1.286e+01	8.774e-03	4.892e+02	1.334e-07	1.904e+04	3.071e-12
1.636e-01	7.641e-03	1.070e+00	4.648e-01	1.402e+01	6.821e-03	5.385e+02	1.002e-07	2.097e+04	2.318e-12
1.717e-01	8.714e-03	1.128e+00	4.837e-01	1.529e+01	5.286e-03	5.929e+02	7.541e-08	2.309e+04	1.749e-12
1.802e-01	9.938e-03	1.189e+00	5.020e-01	1.669e+01	4.083e-03	6.527e+02	5.677e-08	2.543e+04	1.319e-12
1.891e-01	1.134e-02	1.255e+00	5.191e-01	1.823e+01	3.143e-03	7.187e+02	4.277e-08	2.800e+04	9.955e-13
1.985e-01	1.293e-02	1.324e+00	5.340e-01	1.993e+01	2.412e-03	7.913e+02	3.224e-08	3.084e+04	7.511e-13
2.084e-01	1.476e-02	1.399e+00	5.458e-01	2.179e+01	1.845e-03	8.712e+02	2.432e-08	3.396e+04	5.666e-13
2.187e-01	1.685e-02	1.478e+00	5.538e-01	2.384e+01	1.408e-03	9.593e+02	1.836e-08	3.740e+04	4.275e-13
2.296e-01	1.923e-02	1.563e+00	5.576e-01	2.610e+01	1.071e-03	1.056e+03	1.386e-08	4.118e+04	3.225e-13
2.410e-01	2.196e-02	1.653e+00	5.566e-01	2.859e+01	8.132e-04	1.163e+03	1.047e-08	4.535e+04	2.433e-13
2.529e-01	2.508e-02	1.750e+00	5.507e-01	3.133e+01	6.157e-04	1.281e+03	7.909e-09	4.994e+04	1.835e-13
2.655e-01	2.864e-02	1.854e+00	5.396e-01	3.434e+01	4.650e-04	1.410e+03	5.977e-09	5.500e+04	1.384e-13
2.787e-01	3.273e-02	1.966e+00	5.234e-01	3.766e+01	3.505e-04	1.553e+03	4.517e-09	6.057e+04	1.044e-13
2.926e-01	3.741e-02	2.086e+00	5.025e-01	4.132e+01	2.636e-04	1.710e+03	3.414e-09	6.670e+04	7.875e-14
3.072e-01	4.277e-02	2.215e+00	4.773e-01	4.534e+01	1.980e-04	1.883e+03	2.580e-09	7.345e+04	5.940e-14
3.225e-01	4.891e-02	2.354e+00	4.484e-01	4.977e+01	1.485e-04	2.073e+03	1.951e-09	8.089e+04	4.480e-14
3.386e-01	5.594e-02	2.505e+00	4.168e-01	5.465e+01	1.114e-04	2.283e+03	1.474e-09	8.908e+04	3.379e-14
3.555e-01	6.400e-02	2.668e+00	3.833e-01	6.003e+01	8.343e-05	2.514e+03	1.115e-09	9.810e+04	2.549e-14
3.733e-01	7.326e-02	2.844e+00	3.490e-01	6.594e+01	6.243e-05	2.768e+03	8.427e-10	1.080e+05	1.922e-14
3.920e-01	8.396e-02	3.034e+00	3.147e-01	7.246e+01	4.669e-05	3.048e+03	6.370e-10	1.190e+05	1.450e-14
4.116e-01	9.622e-02	3.241e+00	2.810e-01	7.963e+01	3.488e-05	3.357e+03	4.815e-10	1.310e+05	1.094e-14
4.323e-01	1.101e-01	3.466e+00	2.485e-01	8.753e+01	2.604e-05	3.696e+03	3.639e-10	1.443e+05	8.248e-15
4.540e-01	1.251e-01	3.711e+00	2.177e-01	9.623e+01	1.942e-05	4.070e+03	2.750e-10	1.589e+05	6.218e-15

Note.^a Differential intensity units: (m² s sr GV)⁻¹.

(This table is available in its entirety in machine-readable form.)

up, even though all models are tuned to the observed secondary-to-primary nuclei ratio, typically B/C.

Therefore, the obtained overall agreement in the description of the spectra of lithium, beryllium, boron, and nitrogen in the framework of the same model that was applied to CR protons, He, C, and O is quite spectacular. The systematic over-production of beryllium at low energies and a deficit of lithium at high energies cannot be cured through the adjustment of other parameters and therefore have to be taken seriously. In the case of beryllium, the most likely reason for the discrepancy is the uncertainties in the total inelastic cross sections of beryllium isotopes, whose uncertainty is comparable with the value of the observed discrepancy between model predictions and CR observations and is most pronounced in the energy range below ~ 10 GeV n⁻¹. The remarkable excess of lithium at high energies $\gtrsim 4$ GV is likely to be of a different origin. It is observed in the energy range where the solar

modulation is moderate or negligible, while all involved cross sections become energy-independent. It is, therefore, likely that we see a signature of a new process.

Recent observations of the ⁷Be lines in the spectra of novae imply that primary ⁷Li should also be present in the ejecta. The peculiar injection spectrum of primary ⁷Li as derived from the fit to the data (Table 1) may be an indication of its non-standard origin. In the injection spectrum of ⁷Li, one can distinguish two different components: the low-energy one that has a steep spectrum between ~ 12 GV and 350 GV with index of 2.7, and the flat-spectrum high-energy component with index ~ 1.9 . The value of the index break 0.8 ± 0.06 at $R_2 = 355 \pm 15$ GV is the largest among the species shown in Table 1. The low-energy part can thus be attributed to the acceleration in the nova shock, while the flat high-energy part with a universal injection index of 2 may come from acceleration of the ejected primary lithium by a SNR shell. Such an interpretation, if

Table 5
Boron LIS

Rigidity GV	Differential Intensity ^a	Rigidity GV	Differential Intensity ^a	Rigidity GV	Differential Intensity ^a	Rigidity GV	Differential Intensity ^a	Rigidity GV	Differential Intensity ^a
9.498e-02	4.269e-03	5.996e-01	5.957e-01	5.000e+00	3.198e-01	1.463e+02	1.438e-05	5.635e+03	3.042e-10
9.968e-02	4.902e-03	6.298e-01	6.625e-01	5.365e+00	2.671e-01	1.609e+02	1.072e-05	6.205e+03	2.300e-10
1.046e-01	5.571e-03	6.617e-01	7.306e-01	5.764e+00	2.216e-01	1.770e+02	7.987e-06	6.833e+03	1.739e-10
1.098e-01	6.332e-03	6.953e-01	7.991e-01	6.199e+00	1.827e-01	1.947e+02	5.954e-06	7.525e+03	1.315e-10
1.152e-01	7.199e-03	7.306e-01	8.673e-01	6.676e+00	1.498e-01	2.142e+02	4.441e-06	8.287e+03	9.938e-11
1.209e-01	8.186e-03	7.679e-01	9.348e-01	7.196e+00	1.221e-01	2.357e+02	3.314e-06	9.125e+03	7.511e-11
1.269e-01	9.310e-03	8.071e-01	1.001e+00	7.767e+00	9.895e-02	2.593e+02	2.475e-06	1.005e+04	5.676e-11
1.332e-01	1.059e-02	8.486e-01	1.065e+00	8.392e+00	7.976e-02	2.854e+02	1.850e-06	1.107e+04	4.289e-11
1.397e-01	1.205e-02	8.923e-01	1.128e+00	9.077e+00	6.391e-02	3.141e+02	1.384e-06	1.219e+04	3.241e-11
1.467e-01	1.372e-02	9.384e-01	1.190e+00	9.829e+00	5.096e-02	3.457e+02	1.036e-06	1.342e+04	2.448e-11
1.539e-01	1.561e-02	9.871e-01	1.250e+00	1.065e+01	4.046e-02	3.805e+02	7.770e-07	1.478e+04	1.849e-11
1.615e-01	1.778e-02	1.039e+00	1.308e+00	1.156e+01	3.199e-02	4.188e+02	5.832e-07	1.627e+04	1.397e-11
1.695e-01	2.024e-02	1.093e+00	1.365e+00	1.256e+01	2.518e-02	4.610e+02	4.383e-07	1.792e+04	1.055e-11
1.779e-01	2.306e-02	1.151e+00	1.420e+00	1.365e+01	1.974e-02	5.074e+02	3.297e-07	1.974e+04	7.969e-12
1.867e-01	2.627e-02	1.212e+00	1.474e+00	1.485e+01	1.540e-02	5.586e+02	2.483e-07	2.173e+04	6.018e-12
1.960e-01	2.993e-02	1.276e+00	1.525e+00	1.617e+01	1.198e-02	6.149e+02	1.871e-07	2.394e+04	4.544e-12
2.057e-01	3.410e-02	1.345e+00	1.573e+00	1.763e+01	9.281e-03	6.770e+02	1.411e-07	2.636e+04	3.431e-12
2.158e-01	3.887e-02	1.418e+00	1.616e+00	1.923e+01	7.169e-03	7.453e+02	1.065e-07	2.903e+04	2.591e-12
2.265e-01	4.431e-02	1.495e+00	1.650e+00	2.098e+01	5.521e-03	8.206e+02	8.047e-08	3.197e+04	1.956e-12
2.378e-01	5.051e-02	1.577e+00	1.674e+00	2.292e+01	4.239e-03	9.035e+02	6.081e-08	3.520e+04	1.477e-12
2.496e-01	5.760e-02	1.665e+00	1.685e+00	2.505e+01	3.245e-03	9.947e+02	4.597e-08	3.877e+04	1.115e-12
2.619e-01	6.568e-02	1.758e+00	1.680e+00	2.739e+01	2.476e-03	1.095e+03	3.476e-08	4.269e+04	8.415e-13
2.749e-01	7.491e-02	1.858e+00	1.659e+00	2.998e+01	1.885e-03	1.206e+03	2.630e-08	4.701e+04	6.352e-13
2.886e-01	8.545e-02	1.965e+00	1.620e+00	3.282e+01	1.432e-03	1.328e+03	1.991e-08	5.177e+04	4.795e-13
3.029e-01	9.750e-02	2.078e+00	1.563e+00	3.594e+01	1.085e-03	1.462e+03	1.507e-08	5.701e+04	3.619e-13
3.180e-01	1.113e-01	2.200e+00	1.491e+00	3.939e+01	8.208e-04	1.610e+03	1.140e-08	6.279e+04	2.731e-13
3.338e-01	1.270e-01	2.331e+00	1.405e+00	4.318e+01	6.197e-04	1.773e+03	8.631e-09	6.914e+04	2.062e-13
3.504e-01	1.450e-01	2.471e+00	1.310e+00	4.735e+01	4.671e-04	1.952e+03	6.532e-09	7.614e+04	1.556e-13
3.678e-01	1.656e-01	2.622e+00	1.209e+00	5.194e+01	3.515e-04	2.149e+03	4.944e-09	8.385e+04	1.174e-13
3.861e-01	1.891e-01	2.785e+00	1.103e+00	5.700e+01	2.641e-04	2.367e+03	3.743e-09	9.234e+04	8.863e-14
4.054e-01	2.160e-01	2.960e+00	9.977e-01	6.257e+01	1.982e-04	2.606e+03	2.833e-09	1.017e+05	6.689e-14
4.256e-01	2.466e-01	3.149e+00	8.937e-01	6.871e+01	1.486e-04	2.870e+03	2.145e-09	1.120e+05	5.048e-14
4.469e-01	2.815e-01	3.353e+00	7.934e-01	7.546e+01	1.113e-04	3.160e+03	1.623e-09	1.233e+05	3.809e-14
4.693e-01	3.211e-01	3.575e+00	6.976e-01	8.290e+01	8.323e-05	3.480e+03	1.228e-09	1.358e+05	2.875e-14
4.928e-01	3.656e-01	3.815e+00	6.076e-01	9.109e+01	6.222e-05	3.832e+03	9.294e-10	1.496e+05	2.170e-14
5.175e-01	4.152e-01	4.075e+00	5.243e-01	1.001e+02	4.647e-05	4.220e+03	7.031e-10	1.647e+05	1.637e-14
5.435e-01	4.704e-01	4.358e+00	4.483e-01	1.100e+02	3.469e-05	4.647e+03	5.319e-10	1.814e+05	1.235e-14
5.708e-01	5.311e-01	4.665e+00	3.801e-01	1.210e+02	2.587e-05	5.117e+03	4.023e-10	1.997e+05	9.218e-15

Note.^a Differential intensity units: (m² s sr GV)⁻¹.

(This table is available in its entirety in machine-readable form.)

correct, provides remarkable insight into the physics of primordial and stellar nucleosynthesis, and may dramatically change our understanding of the origin of CR species. One can notice that the break in the primary lithium injection spectrum R_2 is at about the same rigidity as that for other species. This could be a chance coincidence due to the uncertainties in the lithium data at and above the break rigidity. Meanwhile, evaluation of uncertainties associated with the primary lithium component may require a dedicated study. Though such a possibility is very exciting, we cannot rule out other possibilities for the observed discrepancy just yet.

Interestingly, the injection (I) and propagation (P) scenarios discussed in Sections 2.3 and 4.1 provide fits of the existing data of a comparable quality. Still, the P -scenario looks preferable, as it does not require individual breaks in the injection spectra of all CR species, but rather one universal break in the diffusion coefficient. A better agreement with the CR anisotropy measurements is also an advantage of the P -

scenario. Meanwhile, the described lithium excess is observed in both scenarios, so it is not a feature associated with one particular propagation model.

Our continuing studies of the LIS of various CR species in the combined framework of two propagation codes, GALPROP and HELMOD, show that it is possible to make a self-consistent model of CR propagation in the Galaxy and the heliosphere. Meanwhile, the increasingly accurate CR data that became available in the last decade uncovered new effects and shed new light on the origin of CR species in the energy range that is deemed as well-studied. The self-consistent approach that was one of the cornerstones in the development of the GALPROP propagation code is the key to discovering such new features, as it does not allow much freedom in fitting particular data sets, while using a self-consistent approach for heliospheric propagation as realized in the HELMOD code ensures that all observed features are real indeed.

Table 6
Nitrogen LIS

Rigidity GV	Differential Intensity ^a	Rigidity GV	Differential Intensity ^a	Rigidity GV	Differential Intensity ^a	Rigidity GV	Differential Intensity ^a	Rigidity GV	Differential Intensity ^a
9.252e-02	1.160e-02	5.840e-01	6.888e-01	4.870e+00	2.867e-01	1.425e+02	2.198e-05	5.489e+03	1.780e-09
9.709e-02	1.299e-02	6.135e-01	7.493e-01	5.226e+00	2.417e-01	1.567e+02	1.662e-05	6.044e+03	1.416e-09
1.019e-01	1.453e-02	6.445e-01	8.130e-01	5.614e+00	2.026e-01	1.724e+02	1.257e-05	6.656e+03	1.128e-09
1.069e-01	1.625e-02	6.772e-01	8.796e-01	6.038e+00	1.689e-01	1.896e+02	9.517e-06	7.330e+03	8.984e-10
1.122e-01	1.817e-02	7.116e-01	9.485e-01	6.502e+00	1.402e-01	2.086e+02	7.213e-06	8.071e+03	7.160e-10
1.178e-01	2.033e-02	7.479e-01	1.019e+00	7.009e+00	1.158e-01	2.296e+02	5.475e-06	8.888e+03	5.708e-10
1.236e-01	2.274e-02	7.862e-01	1.090e+00	7.565e+00	9.522e-02	2.526e+02	4.164e-06	9.788e+03	4.552e-10
1.297e-01	2.543e-02	8.265e-01	1.160e+00	8.174e+00	7.788e-02	2.780e+02	3.175e-06	1.078e+04	3.631e-10
1.361e-01	2.845e-02	8.691e-01	1.228e+00	8.841e+00	6.336e-02	3.059e+02	2.428e-06	1.187e+04	2.898e-10
1.428e-01	3.182e-02	9.140e-01	1.295e+00	9.574e+00	5.130e-02	3.367e+02	1.862e-06	1.307e+04	2.313e-10
1.499e-01	3.558e-02	9.615e-01	1.357e+00	1.038e+01	4.137e-02	3.706e+02	1.433e-06	1.439e+04	1.847e-10
1.573e-01	3.980e-02	1.012e+00	1.414e+00	1.126e+01	3.322e-02	4.079e+02	1.106e-06	1.585e+04	1.475e-10
1.651e-01	4.450e-02	1.065e+00	1.465e+00	1.223e+01	2.657e-02	4.490e+02	8.558e-07	1.746e+04	1.178e-10
1.733e-01	4.976e-02	1.121e+00	1.508e+00	1.329e+01	2.116e-02	4.943e+02	6.643e-07	1.922e+04	9.417e-11
1.819e-01	5.563e-02	1.180e+00	1.544e+00	1.447e+01	1.678e-02	5.441e+02	5.169e-07	2.117e+04	7.527e-11
1.909e-01	6.218e-02	1.243e+00	1.573e+00	1.575e+01	1.326e-02	5.990e+02	4.031e-07	2.331e+04	6.018e-11
2.003e-01	6.949e-02	1.310e+00	1.596e+00	1.717e+01	1.043e-02	6.594e+02	3.149e-07	2.567e+04	4.812e-11
2.102e-01	7.765e-02	1.381e+00	1.609e+00	1.873e+01	8.176e-03	7.260e+02	2.464e-07	2.827e+04	3.849e-11
2.207e-01	8.674e-02	1.456e+00	1.611e+00	2.044e+01	6.386e-03	7.993e+02	1.931e-07	3.114e+04	3.079e-11
2.316e-01	9.687e-02	1.536e+00	1.602e+00	2.232e+01	4.970e-03	8.800e+02	1.516e-07	3.429e+04	2.464e-11
2.431e-01	1.081e-01	1.622e+00	1.581e+00	2.440e+01	3.856e-03	9.689e+02	1.191e-07	3.776e+04	1.972e-11
2.551e-01	1.207e-01	1.713e+00	1.547e+00	2.668e+01	2.983e-03	1.067e+03	9.369e-08	4.158e+04	1.578e-11
2.678e-01	1.347e-01	1.810e+00	1.500e+00	2.920e+01	2.301e-03	1.175e+03	7.379e-08	4.579e+04	1.263e-11
2.811e-01	1.502e-01	1.913e+00	1.442e+00	3.196e+01	1.771e-03	1.293e+03	5.817e-08	5.043e+04	1.011e-11
2.950e-01	1.675e-01	2.024e+00	1.374e+00	3.501e+01	1.360e-03	1.424e+03	4.589e-08	5.553e+04	8.098e-12
3.097e-01	1.866e-01	2.143e+00	1.299e+00	3.836e+01	1.043e-03	1.568e+03	3.623e-08	6.115e+04	6.485e-12
3.251e-01	2.079e-01	2.270e+00	1.217e+00	4.205e+01	7.977e-04	1.727e+03	2.863e-08	6.735e+04	5.194e-12
3.413e-01	2.315e-01	2.407e+00	1.131e+00	4.612e+01	6.091e-04	1.901e+03	2.264e-08	7.416e+04	4.160e-12
3.583e-01	2.576e-01	2.554e+00	1.043e+00	5.059e+01	4.644e-04	2.094e+03	1.791e-08	8.167e+04	3.333e-12
3.761e-01	2.866e-01	2.712e+00	9.527e-01	5.552e+01	3.535e-04	2.305e+03	1.418e-08	8.994e+04	2.670e-12
3.949e-01	3.188e-01	2.883e+00	8.628e-01	6.095e+01	2.688e-04	2.538e+03	1.124e-08	9.905e+04	2.139e-12
4.146e-01	3.542e-01	3.067e+00	7.741e-01	6.692e+01	2.041e-04	2.795e+03	8.909e-09	1.091e+05	1.714e-12
4.353e-01	3.930e-01	3.266e+00	6.885e-01	7.350e+01	1.548e-04	3.078e+03	7.067e-09	1.201e+05	1.374e-12
4.571e-01	4.349e-01	3.482e+00	6.072e-01	8.075e+01	1.174e-04	3.390e+03	5.609e-09	1.323e+05	1.101e-12
4.800e-01	4.797e-01	3.715e+00	5.311e-01	8.872e+01	8.889e-05	3.732e+03	4.454e-09	1.457e+05	8.825e-13
5.040e-01	5.273e-01	3.969e+00	4.606e-01	9.751e+01	6.728e-05	4.110e+03	3.539e-09	1.604e+05	7.073e-13
5.293e-01	5.779e-01	4.244e+00	3.962e-01	1.072e+02	5.089e-05	4.526e+03	2.813e-09	1.767e+05	5.672e-13
5.560e-01	6.317e-01	4.544e+00	3.382e-01	1.178e+02	3.848e-05	4.984e+03	2.237e-09	1.945e+05	4.487e-13

Note.^a Differential intensity units: (m² s sr GV)⁻¹.

(This table is available in its entirety in machine-readable form.)

Special thanks goes to Pavol Bobik, Giuliano Boella, Karel Kudela, Marian Putis, and Mario Zannoni for their continuous support of the HELMOD project and many useful suggestions. This work is supported by ASI (Agenzia Spaziale Italiana) through a contract ASI-INFN I/002/13/0 and by ESA (European Space Agency) through a contract 4000116146/16/NL/HK. Igor Moskalenko and Troy Porter acknowledge support from NASA grant No. NNX17AB48G. We thank the ACE CRIS instrument team and the ACE Science Center for providing the ACE data.

Appendix Supplementary Material

Here we provide analytical fits to the calculated LIS of lithium, beryllium, boron, and nitrogen for the energy range from 350 MV–50 TV, Equations (5)–(8), as well as fully numerical output tables of the LIS from GALPROP, Tables 3–6. The fits are tuned to match the GALPROP-calculated LIS within 1%–5% over five orders of magnitude in rigidity including the spectral flattening at high energies:

$$F_{\text{Li}}(R) \times R^{2.7} = \begin{cases} \frac{104.41R^{-0.24}}{4.50 + 117.73R^{-3.60} + 21.45R^{-6.72}}, & R \leq 2.7 \text{ GV}, \\ 3.11 - \frac{46.22}{R} + \frac{2509.17}{92 + 4.02R} - 1.41 \times 10^{-5}R + 4.73 \times 10^{-11}R^2 + (0.032 - 6.74 \times 10^{-14}R^2)\sqrt{R}, & R > 2.7 \text{ GV}, \end{cases} \quad (5)$$











$$F_{\text{Be}}(R) \times R^{2.7} = \begin{cases} \frac{167.10R^{-0.25}}{15.34 + 313.32R^{-3.61} + 49.18R^{-6.48}}, & R \leq 2.3 \text{ GV}, \\ 0.067 - (4.12 \times 10^{-5} - 3.21 \times 10^{-6} \ln R + 0.18 \times 0.90^R)R + (0.99 - 1.59 \times 0.32^R)e^{\frac{3.16 \ln R}{\sqrt{0.20+R}}}, & R > 2.3 \text{ GV}, \end{cases} \quad (6)$$

$$F_{\text{B}}(R) \times R^{2.7} = \begin{cases} \frac{11.47R^{-0.25}}{0.327 + 7.50R^{-3.67} + 1.21R^{-6.73}}, & R \leq 3 \text{ GV}, \\ 6.90 + \frac{946.97}{61.11 + R} - \frac{606.57 + 37.17\tilde{R}}{R} + \frac{1004.79\tilde{R}}{R + \tilde{R}} + 0.00017R - 9.79 \times 10^{-10}R^2 - 0.0465\tilde{R}, & R > 3 \text{ GV}, \end{cases} \quad (7)$$

$$F_{\text{N}}(R) \times R^{2.7} = \begin{cases} \frac{75.12R^{-0.16}}{2.69 + 29.18R^{-2.75} + 21.81R^{-5.25}}, & R \leq 3.6 \text{ GV}, \\ 281.08 + \frac{65}{1.66 + 1.0072R} + 0.0017R - 0.87\sqrt{R} + (24.5 - 4.19 \times 10^{-5}R)\sqrt[4]{R} - 79.07 \ln(21.52\sqrt[4]{R}), & R > 3.6 \text{ GV}, \end{cases} \quad (8)$$

where $\tilde{R} = \sqrt{1.19 + R}$. The numerical values in the fits and tables correspond to the *I*-scenario, which has more free parameters and, therefore, the fits to the data are more accurate; see Figures 7 and 8.

ORCID iDs

M. J. Boschini  <https://orcid.org/0000-0002-6401-0457>
 S. Della Torre  <https://orcid.org/0000-0002-7669-0859>
 M. Gervasi  <https://orcid.org/0000-0003-3884-0905>
 D. Grandi  <https://orcid.org/0000-0003-1942-8587>
 G. Jøhannesson  <https://orcid.org/0000-0003-1458-7036>
 G. La Vacca  <https://orcid.org/0000-0002-2168-9447>
 N. Masi  <https://orcid.org/0000-0002-3729-7608>
 I. V. Moskalenko  <https://orcid.org/0000-0001-6141-458X>
 T. A. Porter  <https://orcid.org/0000-0002-2621-4440>
 P. G. Rancoita  <https://orcid.org/0000-0002-1990-4283>
 D. Rozza  <https://orcid.org/0000-0002-7378-6353>
 M. Tacconi  <https://orcid.org/0000-0002-9344-6305>

References

- Abraham, P. B., Brunstein, K. A., & Cline, T. L. 1966, *PhRv*, **150**, 1088
 Ackermann, M., Ajello, M., Albert, A., et al. 2014, *PhRvL*, **112**, 151103
 Adriani, O., Barbarino, G. C., Bazilevskaya, G. A., et al. 2011, *Sci*, **332**, 69
 Adriani, O., Barbarino, G. C., Bazilevskaya, G. A., et al. 2014, *ApJ*, **791**, 93
 Aguilar, M., Aisa, D., Alpat, B., et al. 2015a, *PhRvL*, **114**, 171103
 Aguilar, M., Aisa, D., Alpat, B., et al. 2015b, *PhRvL*, **115**, 211101
 Aguilar, M., Ali Cavasonza, L., Alpat, B., et al. 2017, *PhRvL*, **119**, 251101
 Aguilar, M., Ali Cavasonza, L., Alpat, B., et al. 2018a, *PhRvL*, **121**, 051101
 Aguilar, M., Ali Cavasonza, L., Alpat, B., et al. 2018b, *PhRvL*, **121**, 051103
 Aguilar, M., Ali Cavasonza, L., Alpat, B., et al. 2019a, *PhRvL*, **122**, 101101
 Aguilar, M., Ali Cavasonza, L., Ambrosi, G., et al. 2018c, *PhRvL*, **120**, 021101
 Aguilar, M., Ali Cavasonza, L., Ambrosi, G., et al. 2018d, *PhRvL*, **120**, 021101
 Aguilar, M., Ali Cavasonza, L., Ambrosi, G., et al. 2019b, *PhRvL*, **122**, 041102
- Ahn, H. S., Allison, P., Bagliesi, M. G., et al. 2010, *ApJL*, **714**, L89
 Arnould, M., & Norgaard, H. 1975, *A&A*, **42**, 55
 Berezhinskii, V. S., Bulanov, S. V., Dogiel, V. A., & Ptuskin, V. S. 1990, in *Astrophysics of Cosmic Rays*, ed. V. L. Ginzburg (Amsterdam: North-Holland)
 Berrington, R. C., & Dermer, C. D. 2003, *ApJ*, **594**, 709
 Blasi, P., Amato, E., & Serpico, P. D. 2012, *PhRvL*, **109**, 061101
 Bobik, P., Boella, G., Boschini, M. J., et al. 2012, *ApJ*, **745**, 132
 Bobik, P., Boschini, M. J., Della Torre, S., et al. 2016, *JGRA*, **121**, 3920
 Boschini, M. J., Della Torre, S., Gervasi, M., et al. 2017, *ApJ*, **840**, 115
 Boschini, M. J., Della Torre, S., Gervasi, M., et al. 2018a, *ApJ*, **854**, 94
 Boschini, M. J., Della Torre, S., Gervasi, M., et al. 2018b, *ApJ*, **858**, 61
 Boschini, M. J., Della Torre, S., Gervasi, M., La Vacca, G., & Rancoita, P. G. 2018c, *AdSpR*, **62**, 2859
 Boschini, M. J., Della Torre, S., Gervasi, M., La Vacca, G., & Rancoita, P. G. 2019, *AdSpR*, **64**, 2459
 Cameron, A. G. W. 1955, *ApJ*, **121**, 144
 Cameron, A. G. W., & Fowler, W. A. 1971, *ApJ*, **164**, 111
 Crawford, H. J. 1979, PhD thesis, Univ. California Berkeley
 Cummings, A. C., Stone, E. C., Heikkilä, B. C., et al. 2016, *ApJ*, **831**, 18
 de Nolfo, G. A., Moskalenko, I. V., Binns, W. R., et al. 2006, *AdSpR*, **38**, 1558
 Dermer, C. D. 1986a, *A&A*, **157**, 223
 Dermer, C. D. 1986b, *ApJ*, **307**, 47
 Di Felice, V., Pizzolotto, C., D'Urso, D., et al. 2017, ICRC (Busan), **301**, 1073
 Engelmann, J. J., Ferrando, P., Soutoul, A., et al. 1990, *A&A*, **233**, 96
 Génolini, Y., Maurin, D., Moskalenko, I. V., & Unger, M. 2018, *PhRvC*, **98**, 034611
 Génolini, Y., Serpico, P. D., Boudaud, M., et al. 2017, *PhRvL*, **119**, 241101
 Hernanz, M. 2015, *Natur*, **518**, 307
 Hernandez, M., Jose, J., Coc, A., & Isern, J. 1996, *ApJL*, **465**, L27
 Izzo, L., Della Valle, M., Mason, E., et al. 2015, *ApJL*, **808**, L14
 Izzo, L., Molaro, P., Bonifacio, P., et al. 2018, *MNRAS*, **478**, 1601
 Jóhannesson, G., Porter, T. A., & Moskalenko, I. V. 2018, *ApJ*, **856**, 45
 Jóhannesson, G., Porter, T. A., & Moskalenko, I. V. 2019, *ApJ*, **879**, 91
 Jóhannesson, G., Ruiz de Austri, R., Vincent, A. C., et al. 2016, *ApJ*, **824**, 16
 Jones, F. C., Lukasiak, A., Ptuskin, V. S., & Webber, W. R. 2001, *AdSpR*, **27**, 737
 Kachelriess, M., Moskalenko, I. V., & Ostapchenko, S. 2019, *CoPhC*, **245**, 106846
 Kachelriess, M., Moskalenko, I. V., & Ostapchenko, S. S. 2014, *ApJ*, **789**, 136
 Kachelriess, M., Moskalenko, I. V., & Ostapchenko, S. S. 2015, *ApJ*, **803**, 54

- Kachelrieß, M., & Ostapchenko, S. 2012, *PhRvD*, **86**, 043004
- Kamae, T., Karlsson, N., Mizuno, T., Abe, T., & Koi, T. 2006, *ApJ*, **647**, 692
- Kawanaka, N., & Yanagita, S. 2018, *PhRvL*, **120**, 041103
- Lave, K. A., Wiedenbeck, M. E., Binns, W. R., et al. 2013, *ApJ*, **770**, 117
- Malkov, M. A., Diamond, P. H., & Sagdeev, R. Z. 2012, *PhPl*, **19**, 082901
- Mashnik, S. G., Gudima, K. K., Moskalenko, I. V., Prael, R. E., & Sierk, A. J. 2004, *AdSpR*, **34**, 1288
- Masi, N. 2016, *Il Nuovo Cimento C*, **39**, 282
- Moskalenko, I. V., Jóhannesson, G., Orlando, E., Porter, T. A., & Strong, A. W. 2017, *ICRC (Busan)*, **35**, 279
- Moskalenko, I. V., & Jourdain, E. 1997, *A&A*, **325**, 401
- Moskalenko, I. V., & Mashnik, S. G. 2003, *ICRC (Tsukuba)*, **4**, 1969
- Moskalenko, I. V., Mashnik, S. G., & Strong, A. W. 2001, *ICRC (Hamburg)*, **5**, 1836
- Moskalenko, I. V., & Strong, A. W. 1998, *ApJ*, **493**, 694
- Moskalenko, I. V., & Strong, A. W. 2000, *ApJ*, **528**, 357
- Moskalenko, I. V., Strong, A. W., Mashnik, S. G., & Ormes, J. F. 2003, *ApJ*, **586**, 1050
- Moskalenko, I. V., Strong, A. W., Ormes, J. F., & Potgieter, M. S. 2002, *ApJ*, **565**, 280
- Moskalenko, I. V., Strong, A. W., & Reimer, O. 1998, *A&A*, **338**, L75
- Niebur, S. M., Scott, L. M., Wiedenbeck, M. E., et al. 2003, *JGRA*, **108**, 8033
- Niu, J.-S., Li, T., & Xue, H.-F. 2019, *ApJ*, **873**, 77
- Orlando, E., & Strong, A. 2013, *MNRAS*, **436**, 2127
- Panov, A. D., Adams, J. H., Ahn, H. S., et al. 2009, *BRASP*, **73**, 564
- Parker, E. N. 1961, *ApJ*, **134**, 20
- Parker, E. N. 1963, *Interplanetary Dynamical Processes* (New York: Interscience)
- Parker, E. N. 1965, *P&SS*, **13**, 9
- Porter, T. A., Jóhannesson, G., & Moskalenko, I. V. 2017, *ApJ*, **846**, 67
- Porter, T. A., Jóhannesson, G., & Moskalenko, I. V. 2019, *ApJ*, **887**, 250
- Porter, T. A., Moskalenko, I. V., Strong, A. W., Orlando, E., & Bouchet, L. 2008, *ApJ*, **682**, 400
- Pratt, R. H., Ron, A., & Tseng, H. K. 1973, *RvMP*, **45**, 273
- Press, W. H., Teukolsky, S. A., Vetterling, W. T., & Flannery, B. P. 1992, *Numerical Recipes in FORTRAN. The Art of Scientific Computing* (Cambridge: Cambridge Univ. Press)
- Ptuskin, V. S., Jones, F. C., Seo, E. S., & Sina, R. 2006a, *AdSpR*, **37**, 1909
- Ptuskin, V. S., Moskalenko, I. V., Jones, F. C., Strong, A. W., & Zirakashvili, V. N. 2006b, *ApJ*, **642**, 902
- Ptuskin, V. S., & Soutoul, A. 1998, *A&A*, **337**, 859
- Schael, S., Atanasyan, A., Berdugo, J., et al. 2019, *NIMPA*, **944**, 162561
- Selvelli, P., Molaro, P., & Izzo, L. 2018, *MNRAS*, **481**, 2261
- Seo, E. S., & Ptuskin, V. S. 1994, *ApJ*, **431**, 705
- Silberberg, R., Tsao, C. H., & Barghouty, A. F. 1998, *ApJ*, **501**, 911
- Soutoul, A., Legrain, R., Lukasiak, A., McDonald, F. B., & Webber, W. R. 1998, *A&A*, **336**, L61
- Starrfield, S., Truran, J. W., Sparks, W. M., & Arnould, M. 1978, *ApJ*, **222**, 600
- Stone, E. C., Cummings, A. C., Heikkilä, B. C., & Lal, N. 2019, *NatAs*, **3**, 1013
- Strong, A. W., & Moskalenko, I. V. 1998, *ApJ*, **509**, 212
- Strong, A. W., & Moskalenko, I. V. 2001, *AdSpR*, **27**, 717
- Strong, A. W., Moskalenko, I. V., & Ptuskin, V. S. 2007, *ARNPS*, **57**, 285
- Strong, A. W., Moskalenko, I. V., & Reimer, O. 2000, *ApJ*, **537**, 763
- Strong, A. W., Moskalenko, I. V., & Reimer, O. 2004, *ApJ*, **613**, 962
- Strong, A. W., Orlando, E., & Jaffe, T. R. 2011, *A&A*, **534**, A54
- Strong, A. W., Porter, T. A., Digel, S. W., et al. 2010, *ApJL*, **722**, L58
- Sveshnikova, L. G., Strelnikova, O. N., & Ptuskin, V. S. 2013, *Aph*, **50**, 33
- Tajitsu, A., Sadakane, K., Naito, H., et al. 2016, *ApJ*, **818**, 191
- Tajitsu, A., Sadakane, K., Naito, H., Arai, A., & Aoki, W. 2015, *Natur*, **518**, 381
- Tan, L. C., & Ng, L. K. 1983a, *JPhG*, **9**, 1289
- Tan, L. C., & Ng, L. K. 1983b, *JPhG*, **9**, 227
- Trotta, R., Jóhannesson, G., Moskalenko, I. V., et al. 2011, *ApJ*, **729**, 106
- Vladimirov, A. E., Digel, S. W., Jóhannesson, G., et al. 2011, *CoPhC*, **182**, 1156
- Vladimirov, A. E., Jóhannesson, G., Moskalenko, I. V., & Porter, T. A. 2012, *ApJ*, **752**, 68
- Webber, W. R., & Soutoul, A. 1998, *ApJ*, **506**, 335
- Webber, W. R., Soutoul, A., Kish, J. C., & Rockstroh, J. M. 2003, *ApJS*, **144**, 153
- Wefel, J. P., Adams, J. H., Ahn, H. S., et al. 2008, *ICRC (Mérida)*, **2**, 31
- Wellisch, H. P., & Axen, D. 1996, *PhRvC*, **54**, 1329
- Wilson, L. W. 1978, PhD thesis, Univ. California Berkeley
- Yoon, Y. S., Ahn, H. S., Allison, P. S., et al. 2011, *ApJ*, **728**, 122